2015

Design of Scattering Scanning Near-Field Optical Microscope

Dustin Schrecongost

DESIGN OF SCATTERING SCANNING NEAR-FIELD OPTICAL MICROSCOPE

Dustin Schrecongost

Thesis submitted
to the Eberly College of Arts and Sciences
at West Virginia University

in partial fulfillment of the requirements for the degree of

Master of Science in
Physics

Cheng Cen, Ph.D., Chair
Aldo Romero, Ph.D.
Mikel Holcomb, Ph.D.

Department of Physics & Astronomy

Morgantown, West Virginia

2015

Keywords: SNOM, near-field, optical microscope, plasmonics

ABSTRACT

Design of Scattering Scanning Near-Field Optical Microscope

Dustin Schrecongost

The primary objective of this work is to construct a fully functional scattering type Scanning Near-field Optical Microscope (s-SNOM), and to understand the working mechanisms behind it. An s-SNOM is an instrument made up of two separate instruments working in unison. One instrument is a scanning optical microscope focusing light onto a raster scanning sample surface combined with an interferometer set up. The second instrument is an Atomic Force Microscope (AFM) operating in noncontact mode. The AFM uses a small probe that interacts with the raster scanning sample surface to map out the topography of the of the sample surface. An s-SNOM uses both of these instruments simultaneously by focusing the light of the optical microscope onto the probe of the AFM. This probe acts as a nano-antenna and confines the light allowing for light-matter interaction to be inferred far below the resolution of the diffraction limit of light. This specific s-SNOM system is unique to others by having a controllable environment. It is high vacuum compatible and variable temperature. In addition, it is efficient at collecting scattered light due to the focusing objective being a partial elliptical mirror which collects 360^{o} of light around the major axis. This s-SNOM system will be used for direct imaging of surface plasmons. Intended works are inducing surface plasmons on InSe thin films, and seeing the enhancement effect of introducing Au nano-rods. Also dielectric properties of materials will be interpreted such as the metal to insulator phase transition of NbO_2.

ACKNOWLEDGEMENTS

I would like to thank many people for helping me achieve this thesis. My committee chair, Professor Cheng Cen, has taught me more about Physics than I ever could have imagined. She has been an excellent mentor and has taught me skills that will benefit me for the rest of my life. Without her expertise this thesis would never have been possible. I would like to thank Professor Aldo Romero for encouraging me to move forward in my education and begin my research right away. Your advice on both education and life has helped me get to where I am today. I am also grateful to Professor Mikel Holcomb for serving on my defense committee on short notice. She had a major influence on me choosing WVU for graduate school just by her demeanor on my campus tour with her. I also need to thank my fellow research assistant Sanjay Adhikari. We spent many days in the lab together, and I believe we helped each other very much on our separate projects while also keeping each other sane in the lab.

Much appreciation is also given to my friends Theodore Lane and Gary Lander at WVU. I had the privilege of having friends going through similar curriculums, and it helped having people who understood my day at work. A special thank you goes to my family. I would not have ever been here in the first place without the support of my parents, Mark Schrecongost and Michele Schrecongost, and my sister, Danielle DeBiasio. One cannot get to the present without having a past. One more thank you I need to give is to my significant other, Emily Haddix. Without you I would have not had the motivation to achieve this thesis. You have been my drive and shoulder to lean on every step of the way.

TABLE OF CONTENTS

1. INTRODUCTION

"Light is our primary source of information about the environment which surrounds us [1]." It provides fingerprints of the materials it interacts with. The problem with most optical experiments is the overall spatial resolution. The diffraction limit of light limits the spatial resolution to approximately λ/2, while atomic distances are typically on the order of a few angstroms [2]. Thus the area under investigation in most optical experiments is made up of large amounts of particles. By achieving greater spatial resolution, properties of smaller structures within a material have a greater potential for being understood and characterized.

An emerging technique for analyzing light-matter interaction with greater resolution is scattering scanning near-field optical microscopy (s-SNOM). This technique combines two well-known instruments, a scanning optical microscope and an atomic force microscope (AFM), and uses them simultaneously. Atomic force microscopy is a form of scanning probe microscopy which utilizes a sharp, metallic, probing tip to interact with a sample at the surface. Light is focused from the optical microscope onto the metallic tip of the AFM at the sample surface which confines the light proportional to the size of the tip apex radius of curvature within the near-field approximation of light-matter interaction. The light can then interact with the sample surface with spatial resolution that is wavelength independent [1]. The limiting factor is the size of the tip that can be made. A typical tip apex radius of curvature is a few 10's of nanometers. The idea of breaking the diffraction limit light for obtaining high resolution optical images was first proposed by E. H. Synge in 1928. However, experimental realization of this was not until the 1980's when multiple groups developed

aperture based SNOM systems. Then in the 1990's s-SNOM was finally successfully utilized [3].

This thesis will be focused on an s-SNOM system built that gives great versatility. It will go over both the instruments that make up this s-SNOM system, a scanning optical microscope and an AFM, in chapters 2 and 3. This will lead into the s-SNOM system itself in chapter 4. A detailed description of the instrument, theory, uses, and results obtained will be given.

A unique feature to this specific s-SNOM is the ability to function in a wide range of environmental conditions. Each instrument, optical microscope, AFM, and s-SNOM system, are high vacuum and variable temperature compatible. The current setup operates at 10^{-5} mbar. The setup currently has not been used for variable temperatures but is setup to include this feature in the future. The goal is to reach low temperatures of approximately 10 K. These features allow an already sophisticated system to explore pressure and temperature surface optical effects.

This s-SNOM system is also compatible with applied voltages. One capability is to apply a voltage bias from the cantilever tip of the AFM to the sample surface. Also the samples are mounted on a 5 mm x 5 mm, 28 pin chip carrier. The pins are wired for applying voltages to the sample itself for testing electrical characteristics.

2. SCANNING OPTICAL MICROSCOPE

2.1. Light-Matter Interaction

Light-matter interaction is one of the most popular ways of studying material characteristics. Even as early as 1621, Willebrord Snell stated the well-known Snell's Law:

$$n_1 \sin(\theta_1) = n_2 \sin(\theta_2) \qquad (2.1.1)$$

Where n is the refractive index of a medium, θ_1 is the incident angle of light, and θ_2 is the transmitted angle of light [4]. This law describes that light transmitted from one medium to another will be refracted, and the angle change of the light is related to the refractive indices of the two mediums. The world of optics has come a long way since Snell's Law. Now more sophisticated techniques are employed to gain insight into material characteristics.

One of the main techniques to employ is to inspect the light scattered from atoms. This scattered light could be elastic or inelastic. In the case of elastic scattering the energy of the incident photons is conserved, and the outgoing photons have the same energy as the incident [5]. The most well-known case of elastic scattering is Rayleigh scattering in which light, an electromagnetic field, is scattered off a small particle. The electromagnetic field associated with the light polarizes the particle causing there to be an induced dipole moment that radiates at the frequency of the incident field. This radiating dipole emits light of the same energy based on the wavelength of light which we call scattering [6].

Inelastic scattering is a much more useful phenomenon for gaining knowledge about a material. Inelastic scattering does not have incoming and outgoing photons of the same kinetic energy and thus what happened to that energy tells characteristics of the material. One example of this is Raman scattering which is very similar to Rayleigh scattering. An incident electromagnetic field, light, is incident on the material and induces an oscillating dipole moment [7]:

$$E = E_0 \cos(2\pi \nu_0 t) \qquad (2.1.2)$$

$$P = \alpha\, E_0 \cos(2\pi \nu_0 t) \qquad (2.1.3)$$

Where:

E_0 = electric field amplitude

ν_0 = incident field frequency

t = time

P = dipole moment

α = polarizabilty

For any molecular bond, there are specific quantized vibrational modes or vibrational energy levels. This vibration physically moves atoms about their equilibrium position. These vibrational energy levels and the distance atoms are displaced from equilibrium are defined as [7]:

$$E_{vib} = \left(j + \frac{1}{2}\right) h\nu_{vib} \qquad (2.1.4)$$

$$dX = X_0 \cos(2\pi v_{vib} t) \qquad (2.1.5)$$

Where:

j = quantum number of vibrational mode (0,1,2,...)

h = Planck's constant

v_{vib} = vibrational frequency of mode

dX = displacement from equilibrium position

X_0 = maximum displacement from equilibrium

For small displacements of the atoms, the polarizability of the atoms can be approximated by a Taylor series expansion. Making this approximation and combining it with equations 2.1.3 and 2.1.5 provides the dipole moments induced from the incident light as follows [7]:

$$\alpha = \alpha_0 + \frac{\partial \alpha}{\partial X} dX \qquad (2.1.6)$$

$$P = \alpha_0 E_0 \cos(2\pi v_0 t) + \frac{\partial \alpha}{\partial X} \frac{X_0 E_0}{2} \{\cos[2\pi(v_0 - v_{vib})t] + \cos[2\pi(v_0 + v_{vib})t]\} \qquad (2.1.7)$$

As can be seen from equation 2.1.7, the incident light induces dipole moments at three different frequencies; v_0, v_0-v_{vib}, v_0+v_{vib}. These oscillating dipole moments will scatter photons at these different frequencies. If the scattered photon is at frequency v_0 then it is at the same frequency as the incident photon and the scattering is elastic. This

is the previously mentioned Rayleigh scattering. If the scattered photon frequency is shifted by v_{vib} then it is inelastic Raman scattering. By collecting the scattered light and seeing this frequency shift, the vibrational energy modes can be determined for different materials [8]. C.V. Raman received the Nobel Prize in physics in 1930 for his pioneering of Raman scattering [9].

One more technique of exploring light-matter interaction that is important to touch on is photoluminescence. What happens if the energy of the incoming photons is enough to excite electrons to entirely different energy states? “Photoluminescence is the spontaneous emission of light from a material under optical excitation [10].” Incident photons are absorbed, exciting electrons into different energy levels. The electrons will decay back into the ground state by reemitting a photon. The energy of this emission can be used to determine electron energy states. By employing different incident energies, maps of the electronic structure of materials can be determined. Many different forms of photoluminescence exist such as fluorescence and phosphorescence. Different forms of photoluminescence correspond to different paths of electron excitation and decay [10].

2.2. Principles of Scanning Optical Microscope

A scanning optical microscope is an instrument design used to perform optical measurements on different areas of a sample surface. The base idea is to focus a light source onto the sample surface and then move either the light source or sample in a raster scanning motion. This instrumentation can be set up to probe any light-matter

interaction the experimenter would like to study by changing experimental properties such as the wavelength of the light, light intensity, and polarization.

The main process for scanning optical microscopy is to focus light onto the surface of a sample and have control over the position of the light on the sample. Next either the reflected or transmitted light needs to be collected and formed into a two dimensional map of the sample surface. Figure 2.1 below shows a basic scanning optical microscope setup for collection of the reflected light.

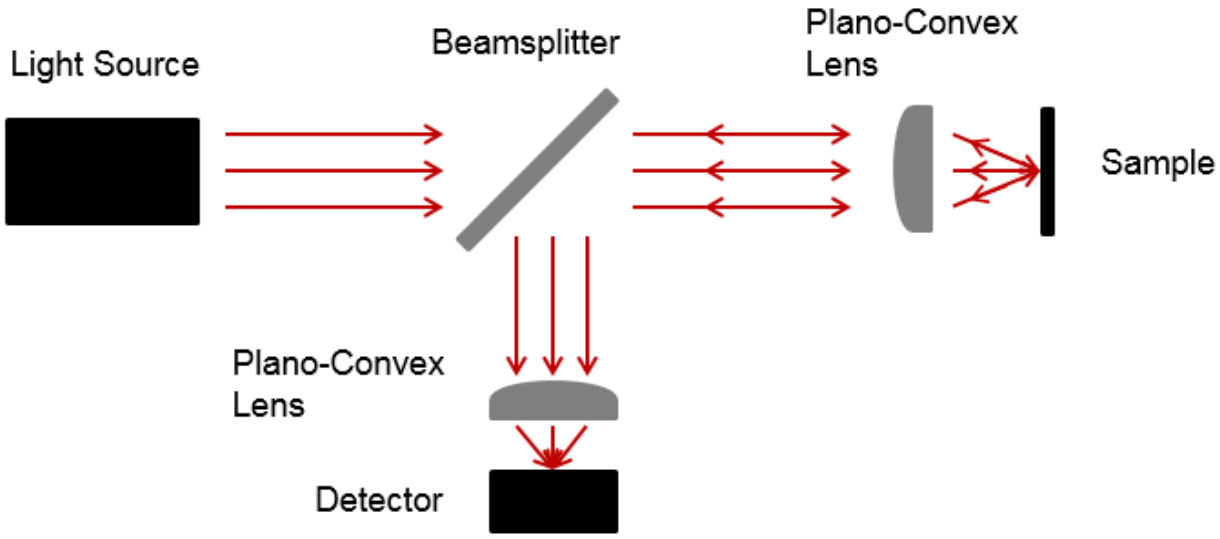

Figure 2.1: Basic implementation of scanning optical microscope

The collimated light passes through a beamsplitter where one half of the light proceeds to the sample surface, and the other half travels elsewhere. This second half of light is not drawn in figure 2.1 and will be discussed and utilized in chapter 4 discussing s-SNOM implementation. The half of light proceeding to the sample is focused onto the sample, reflected light is collected and collimated again, and travels back to the

beamsplitter. When reaching the beamsplitter in the return path, the light is reflected and focused into a photodetector. It is an interferometer setup.

The light or sample needs scanning capability to make this instrument a scanning optical microscope. Typically this is done using piezoelectric actuators. A piezoelectric actuator does a direct conversion of electrical energy into mechanical energy through displacement of the crystal lattice [11]. An applied voltage causes the crystal lattice of the piezoelectric material to expand or compress causing the displacement. Piezoelectric actuators are used for high precision displacements. They have a wide range of capable displacements, but typically they operate from a few microns to multiple hundreds of microns and offer displacement resolution under a nanometer. They have response times on the order of few microseconds [11]. Input voltage requirements vary greatly depending on the characteristics of the specific actuator.

By using piezoelectric actuators to scan the focused light across the sample surface a map or image can be formed of the sample surface for the quantity being tested. This image forming process can be thought of as a series of pictures of the sample surface, and the process is known as raster scanning [12]. The reflection of light is recorded at one spot on the sample surface, the light is moved to the next spot, a second data point is recorded, and this process continues throughout the entire area being scanned. Each data point is essentially a pixel of the map or image. This process is illustrated in figure 2.2.

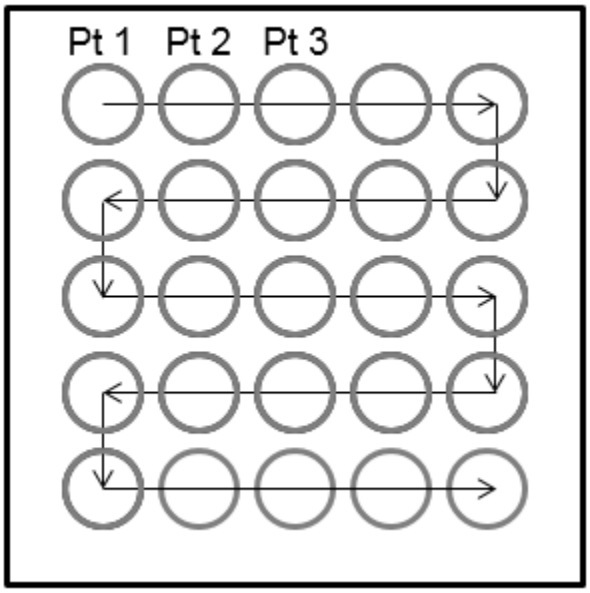

Figure 2.2: Raster scanning dynamics

Scanning optical microscopy is limited in spatial resolution however. Light fundamentally has a diffraction limit which governs the best spatial resolution light can achieve. The best spatial resolution light can achieve naturally is as follows [13]:

$$d_{min} = \frac{\lambda}{2(NA)} = \frac{\lambda}{2(n * sin(\theta))} \qquad (2.2.1)$$

Where:

d_{min} = best spatial resolution or minimum resolvable distance between 2 objects

λ = wavelength of light

NA = numerical aperture

n = refractive index of medium

θ = half aperture angle of objective

Many optical experiments are done with infrared light. If the wavelength of light traveling in air was 10 μm, the best case scenario would be a resolution of 5 μm by maximizing the aperture angle. This resolution is not capable of distinguishing phenomena on an atomic scale.

2.3. Experimental Setup

This section will describe and show the scanning optical microscope central to this thesis. The working principles of it are the same as described in section 2.2 with some modification on the focusing portion of the system. Currently this scanning optical microscope interchanges two lasers depending on the experiment chosen just by placing a mirror on a magnetic mount into or out of the beam path. One laser is a coherent cube laser system. It is a red, direct emitting, diode laser outputting a wavelength of 636 nm at 25 mW. This visible laser is largely used for alignment assistance for the second laser. However it also has materials science applications. For example metals such as Au nanoparticles have surface plasmon resonances near this wavelength which are being explored for signal amplifiers by incorporating the Au nanoparticles on materials [14]. The second laser is a Daylight Solutions Quantum Cascade Laser (QCL). It is a tunable mid-infrared (MIR) laser that can operate as a continuous wave or pulsed laser. It can output a wavelength range of 10.42 μm to 11.17 μm at up to 80 mW. MIR light is essential in materials science. It corresponds to the vibrational energy levels in many materials leading to molecular fingerprints for sensing applications [15]. It also corresponds to the collective oscillation of electrons at interfaces corresponding to surface plasmonics in materials such as graphene [16].

The visible, cube laser, gets passed through an isolator and then is collimated at a larger size making the beam approximately 20 mm in diameter. This increase in diameter will be discussed in chapter 6 discussing problems encountered when implementing this setup. Once collimated the visible light passes through a beamsplitter. Half of the light continues towards the sample, and half of the light is discarded. The light then proceeds to a mirror on a magnetic mount. If this mirror is in place, the visible light is directed to the high vacuum chamber. If the mirror on the magnetic mount is removed, it allows the QCL laser to proceed to the high vacuum chamber. Once inside the chamber, the beam is focused to the sample surface. This will be described more thoroughly in a following paragraph. The light is reflected from the sample surface, collected, and collimated again within the chamber. It then exits the chamber following the same path it entered with. Once the visible light gets back to the beamsplitter it is reflected, and focused to the detector. The visible light detector is a silicon transimpedance amplified detector.

The MIR beam path is similar to the visible laser beam path. It first gets chopped making it an AC signal compatible with the detector amplifier. It is then passed through a 4X beam expander making the beam diameter approximately 10 mm. Next is a beamsplitter allowing half the light to proceed to the high vacuum chamber, and the other half is used as a reference arm which will be utilized for s-SNOM in chapter 4. The MIR light proceeds to the high vacuum chamber, focuses to the sample, and exits the same path. Once proceeding back to the beamsplitter, it is directed and focused to a liquid nitrogen cooled HgCdTe detector. The detector reading is measured using a lock-in amplifier detecting at the chopper frequency.

Both beam paths also include a variety of other optical elements depending on the specific experiment being run. These elements include but are not limited to polarizers, quarter and half wave plates, and neutral density filters. The two beam paths up to the high vacuum chamber are illustrated in figure 2.3 below.

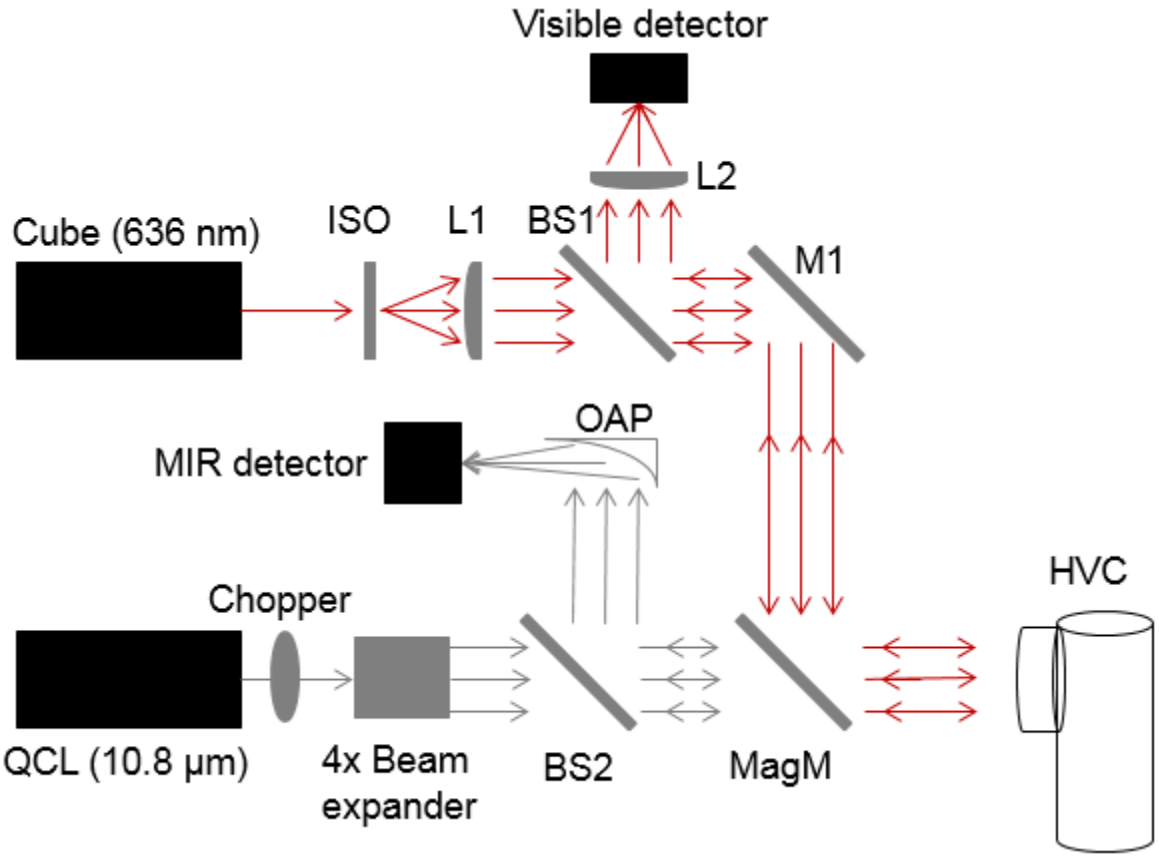

Figure 2.3: Beam paths of MIR and visible lasers; labels are as follow: ISO = isolator, L1 and L2 = plano-convex lenses, M1 = planar silver mirror, BS1 and BS2 = beamsplitters, MagM = planar silver mirror on removable magnetic mount, OAP = off axis parabolic mirror, HVC = high vacuum chamber

The high vacuum chamber has a window on the optical port. This window needs to be transparent to the specific wavelength of light being used. In the case of the visible

light an Al_2O_3 window is used, and a ZnSe window is used for the MIR light. The wavelength dependence on transparency is plotted below for each window in figures 2.4a and 2.4b.

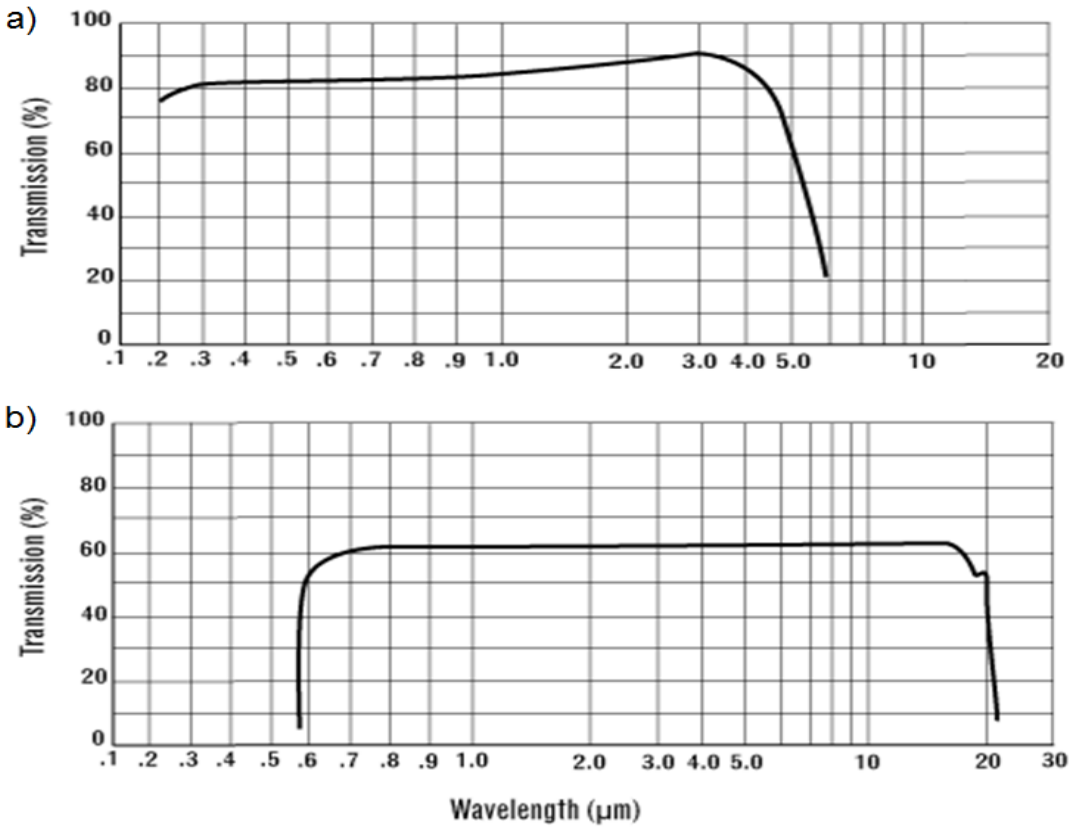

Figure 2.4: Wavelength vs. transmission for a) Al_2O_3 window b) ZnSe window [17]

Once passing through the window, the light reflects off of a 45º planar silver mirror. This mirror directs the light downward. Directly below the 45º mirror is a lens. A common silica, aspheric lens is used for the visible wavelength with NA = 0.543. This lens needs changed for using MIR light to a ZnSe, aspheric lens with NA = 0.67. Below the lens is an elliptical mirror which focuses the light to the sample surface.

Elliptical mirrors have two focal points, and a key feature is that any light passing through one focal point on the way to the mirror will always focus to the second focal point [18]. The sample is placed at the lower focal point of the elliptical mirror. Then the focal point of the lens above is positioned to overlap with the upper focal point of the elliptical mirror. The 45º mirror and lens can be translated and rotated about all three spatial axes using piezoelectric actuators. By achieving this focal point alignment, light is focused to the sample, and any reflected or scattered light is collected by the elliptical mirror and sent back to the upper focal point. The advantage of using an elliptical mirror as the focusing objective is that the light being scattered in any radial direction can be collected by the elliptical mirror. The optical setup of this system inside the high vacuum chamber is shown in figure 2.5.

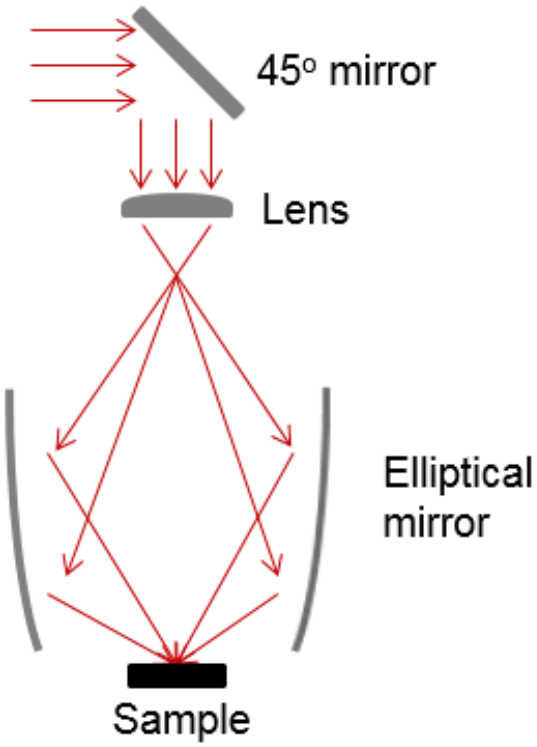

Figure 2.5: Ray diagram inside high vacuum chamber

The sample surface resides at the bottom focal point of the elliptical mirror. The light is incident on the sample at shallows angles allowing for in plane momentum to be introduced to the sample. This allows for the potential of unique experiments such as spin injection using circularly polarized light.

The sample is the component actually being raster scanned in this system. Piezoelectric actuators provide translation along all three spatial axes of the sample. Figures 2.6 provides optical images taken using this system along with the achieved spatial resolution. 636 nm light achieved resolution of approximately 7 µm, and the 10.8 µm light achieved resolution of approximately 30 µm.

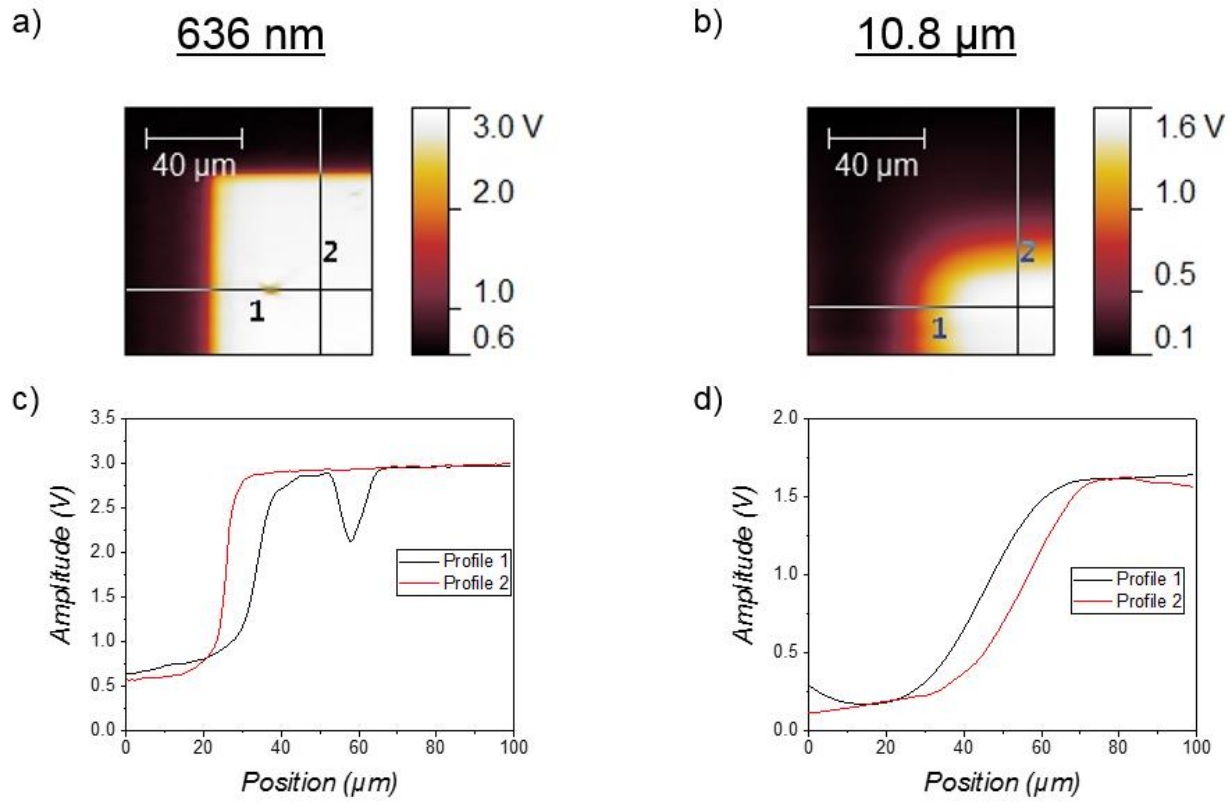

Figure 2.6: Optical images of Au electrode on LAO/STO a) 636 nm b) 10.8 µm, and line profiles 1 and 2 for X and Y directions of optical images c) 636 nm d) 10.8 µm

3. ATOMIC FORCE MICROSCOPE

3.1. Principles of Atomic Force Microscopy

An atomic force microscope (AFM) is a versatile tool for sample surface classification with sub-angstrom resolution by giving quantitative analysis of local forces. The main working principle of an AFM is to measure the force between a sharp probing tip and sample surface [19]. These force measurements have the versatility of working on conducting or insulating materials, which is unique to other instruments such as a scanning tunneling microscope [20]. Sharp probing tips are known as cantilevers, they come in a variety of shapes and sizes. For the purpose of this thesis, cantilevers will be restricted to a basic cantilever design where there is a chip with a rectangular beam out of one end of the chip, and at the end of the beam is a sharp probing tip with apex radius of approximately 30 nm depending on the design. The size of the tip defines the in plane spatial resolution. A cantilever is shown in figure 3.1.

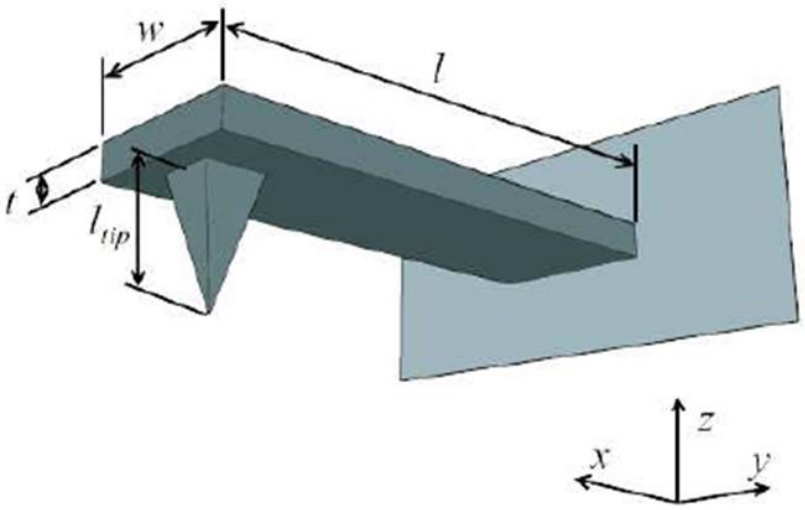

Figure 3.1: Illustration of typical cantilever design [20]

The beam of the cantilever has an associated spring constant, k, and resonant frequency. This spring constant is the key in determining forces by using Hooke's Law, F = - k*d. By knowing the distance that the cantilever is displaced and the spring constant, the force between the cantilever and sample surface can be calculated. As the cantilever is moved closer and closer to the sample surface it primarily is responding to van der Waals forces. There are other variations of scanning probe microscopy designed for probing other forces such as magnetic force microscopy and electrostatic force microscopy, but van der Waals forces are the most frequently used form of measurement [20]. Figure 3.2 shows the force experienced by a cantilever as it approaches the sample surface.

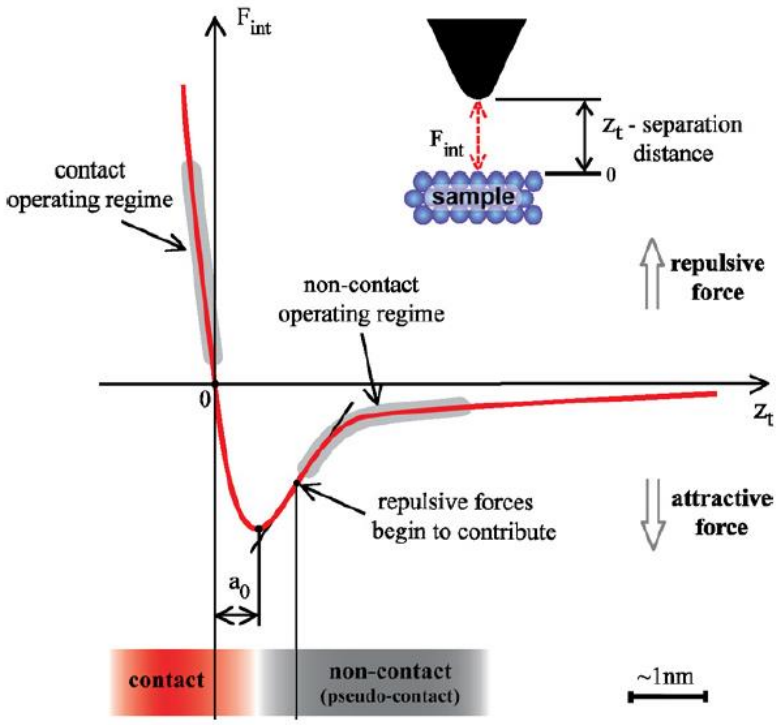

Figure 3.2: Force vs. distance curve as a cantilever is brought into contact with sample surface; Z_t is the distance from tip to surface and a_0 is intermolecular distance [20]

As shown in figure 3.2, at distances far from the sample surface, the cantilever experiences no interaction with the sample. As it moves closer, the cantilever experiences an attractive force, and at an even closer distance the cantilever is in actual contact with the sample surface and experiences a repulsive force.

As previously mentioned force between the tip and sample is determined using Hooke's Law. Each cantilever has a specific spring constant; the key is determining the displacement of the cantilever relative to the sample as they interact. This is done by focusing a laser on the back of the cantilever tip and then placing a 4 quadrant photodetector in the path of the reflected light. When the cantilever tip is within the proximity of interaction, the beam of the cantilever is bent and the reflecting light is moved within the photodetector. This change in intensity between detector quadrants allows for calculation of displacement of the tip. This concept is shown in figure 3.3.

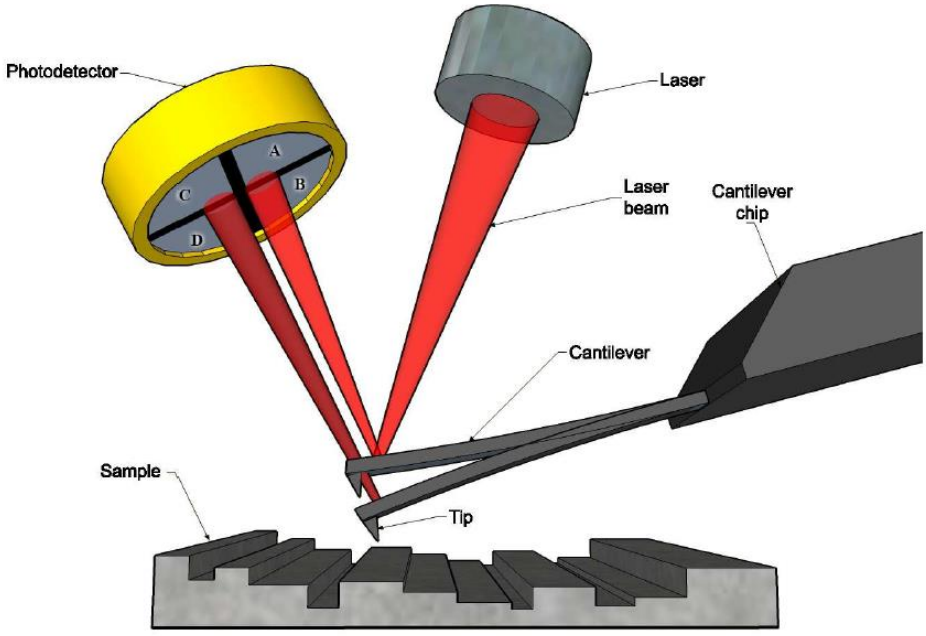

Figure 3.3: Displacement detection of cantilever tip [20]

The sample is raster scanned under the tip, and at each point of the scan, a measurement is taken corresponding to the force at that point. A change in force can be attributed to a change in sample topography or local properties of the material at that point.

An AFM has two primary modes of operation, contact and noncontact. In contact mode, the cantilever tip is brought into contact with the sample surface in the repulsive force regime, and a raster scan is begun. As the cantilever tip is displaced up or down as shown on the photodetector, a feedback loop raises and lowers the sample to maintain a constant force or photodetector ratio between the quadrants as the raster scan is performed [21]. This mode of operation creates high resolution topography images of the sample surface by recording how far the sample had to raise and lower at each point of the raster scan.

The second primary mode of operation, noncontact mode, involves oscillating the cantilever tip at the designed resonant frequency using a piezoelectric actuator. A constant AC voltage is applied to the actuator to create these oscillations. The oscillations have an amplitude, phase, and frequency describing the motion of the cantilever [22]. Interaction with the sample will change these properties creating information on the interaction. The oscillation initially has free air amplitude as seen by the photodetector. As interaction occurs, the oscillation amplitude decreases. A set point is given for the desired amplitude of oscillation for during the raster scan. Then similar to contact mode, a raster scan proceeds, and the sample is moved up and down by a feedback loop that maintains constant amplitude of the cantilever oscillation. Tapping mode offers some advantages to contact mode. One is that there are three

potential quantities for operation of the feedback loop; amplitude, phase, and frequency [22]. All three are affected by the interaction of the tip and sample surface and can be measured simultaneously. A second advantage is that less damage occurs to the tip and sample surface. The tip is not in constant contact with the sample surface in this operating mode [22].

3.2. Experimental Setup

The AFM in this experimental set up is a versatile instrument. It has the advantage of applying electrical biases between the tip and sample, operates in contact and noncontact mode, and is compatible with environmental changes such as temperature and pressure. It has the capability of other forms of scanning probe microscopy as well such as magnetic force microscopy and electrostatic force microscopy. The principles behind this AFM are the same as described in section 3.1. The major difference in this setup compared to the AFM description in section 3.1 is the detection scheme for measuring the displacement of the cantilever. It is an interferometer setup rather than a 4 quadrant photodetector. The interferometer detection scheme directly measures the displacement of the cantilever with the interference of waves rather than the angle of deflection. It is also a more compact design which benefits the overall s-SNOM system to be discussed in chapter 4. The interferometer detection scheme involves placing the back of the cantilever tip normal to and directly in front of an optical fiber. Light from the fiber is half reflected and half transmitted at the end of the fiber. The half that is transmitted reflects off the back of the cantilever tip and back into the fiber where it can interfere with the light that was reflected within the fiber as shown in figure 3.4.

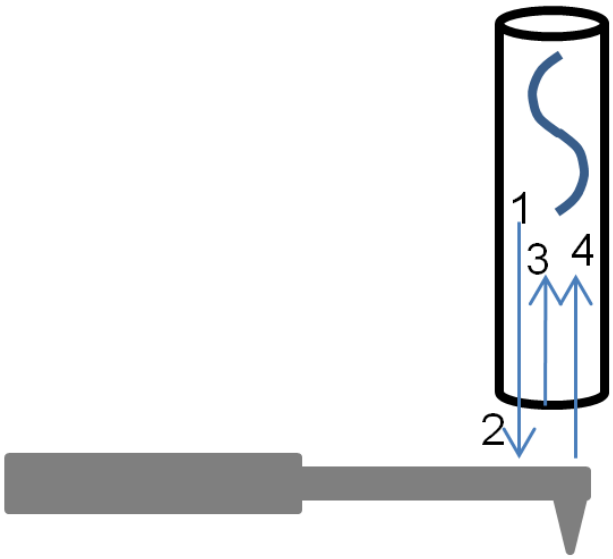

Figure 3.4: Interferometer detection scheme; Beam 1 travels through the fiber to the fiber end where half is transmitted as beam 2 and half is reflected as beam 3. Beam 2 reflects off the end of the cantilever and back into the fiber as beam 4. Beams 3 and 4 interfere traveling back through the fiber.

A piezoelectric actuator known as the quadrature displaces the cantilever with respect to the fiber end and as a result interference fringes are created between the two beams of light returning back through the fiber. This interference is read by a photodetector and is output as a corresponding voltage. These interference fringes correspond to the distance between the cantilever and fiber. A set point for the quadrature is given and a feedback loop maintains this distance within a specified half wavelength range of the fringes. A sweep of the quadrature is shown in figure 3.5.

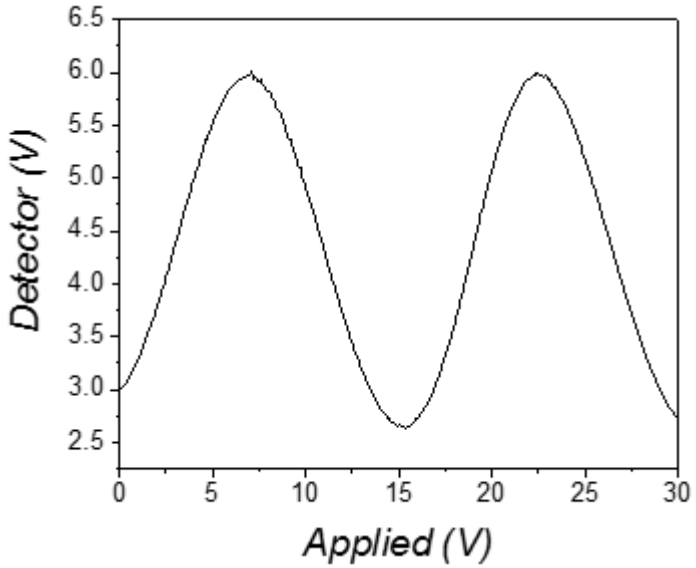

Figure 3.5: Displacement of cantilever tip by quadrature as seen by the photodetector

The set point is chosen to be at maximum slope of the interference fringes. At highest slope, the sensitivity of quadrature position is highest. Small displacements will have a greater change in photodetector reading when the slope is highest.

A second piezoelectric actuator known as the dither is used to oscillate the cantilever at its resonance frequency for noncontact mode measurements. The dither is given a constant drive amplitude and is swept through frequencies to find the resonance frequency of the cantilever. The reflection of light back into the fiber off the cantilever tip is sent through a lock-in amplifier which detects the amplitude of signal at the driving frequency. As the cantilever tip is brought into contact with the sample surface, the oscillation amplitude is decreased due to interaction. A second set point is set for the desired oscillation amplitude which describes the desired force between the tip and sample. Figure 3.6 shows the sweeping of frequencies to find the resonance frequency for in air and in high vacuum.

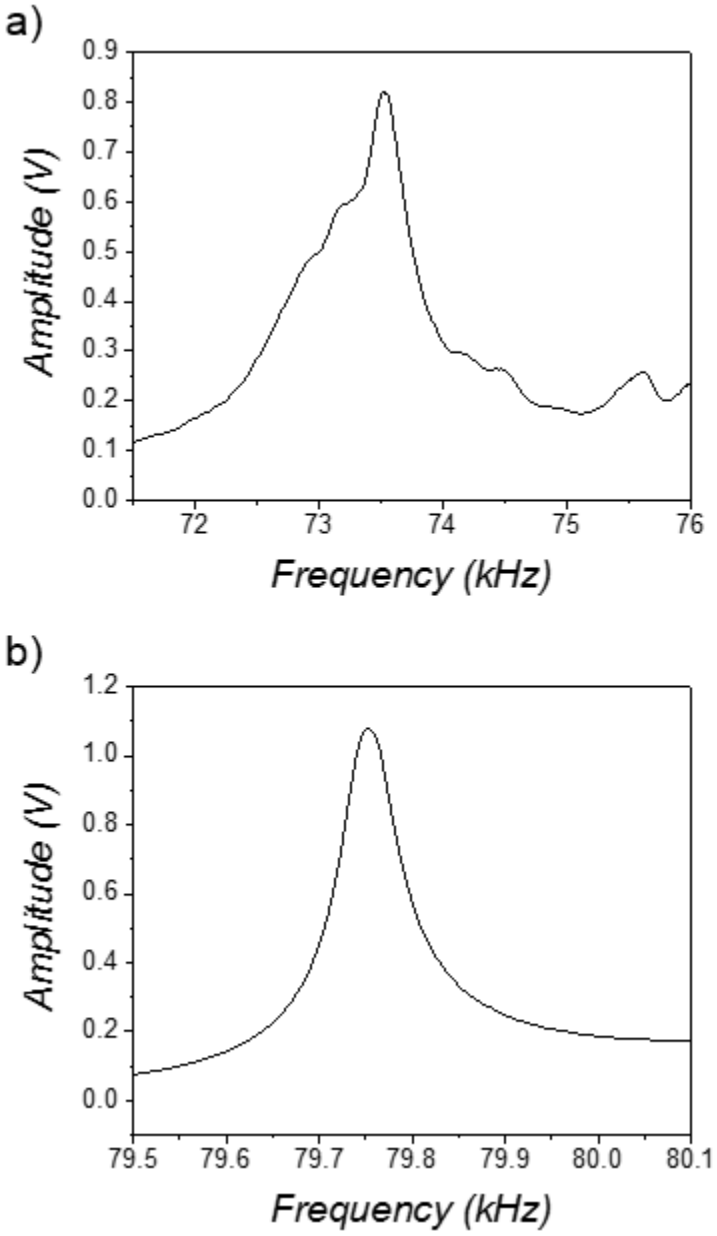

Figure 3.6: Sweep to find the resonance frequency for cantilever oscillation a) in air, Q factor=131, drive amp=45 mV b) in high vacuum, Q factor=1,330, drive amp=0.5 mV

The resonance curve in high vacuum has a much higher Q factor compared to air. Q factor is defined as the ratio of total system energy to dissipation that occurs due to various damping mechanisms. The Q factor can be calculated as [23]:

$$Q = \frac{w_0}{\Delta w} \qquad (3.1.1)$$

Where:

w_0 = resonance frequency

Δw = full width at half maximum of the resonance peak

The Q factor in high vacuum is much higher because of the lack of pressure on the cantilever. The Q factor is inversely proportional to the damping coefficient of an oscillator. Thus by adding air pressure to increase the damping factor, the Q factor decreases. More energy is lost in the system due to air [24].

Once the quadrature and dither have been activated successfully and both reach their designated set point, a raster scan can be initiated. In this system both the cantilever and sample can translate along all three spatial axes by using piezoelectric actuators for experiment locations on the sample. During a raster scan, the sample is the component being moved, and the cantilever is stationary. When scanning in noncontact mode, which is the mode of operation moving forward to s-SNOM, both of the feedback loops for quadrature and dither are turned on. The key is that the dither feedback loop responds much faster, and this needs set in the feedback loop by using standard PID control. This is important so that adjustments are made by just one loop and over compensation by both loops is avoided. Figure 3.7 shows an AFM scan taken in noncontact mode of an Au electrode on LAO/STO. It simultaneously captures topography, the amplitude of cantilever oscillation, and the phase of cantilever oscillation.

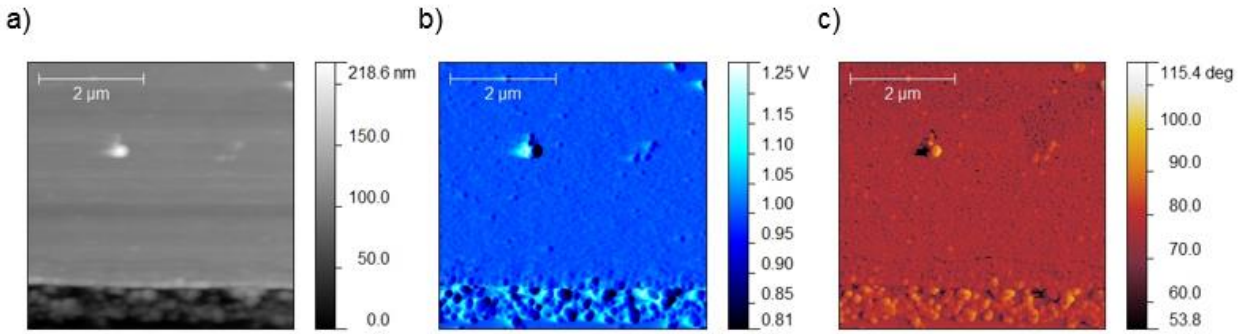

Figure 3.7: Noncontact AFM scan of an Au electrode on LAO/STO a) Topography b) oscillation amplitude c) oscillation phase

4. SCATTERING SCANNING NEAR-FIELD OPTICAL MICROSCOPE

4.1. Principles of Scattering Scanning Near-Field Optical Microscopy

An s-SNOM system is composed of a scanning optical microscope and an AFM. The light of the optical microscope is focused onto the metallic tip apex of the AFM. Therefore the path of the light around the AFM instrumentation must be thought out when designing an s-SNOM system so that as much light as possible can reach the tip. The light path of this s-SNOM inside the high vacuum chamber is shown in figure 4.1.

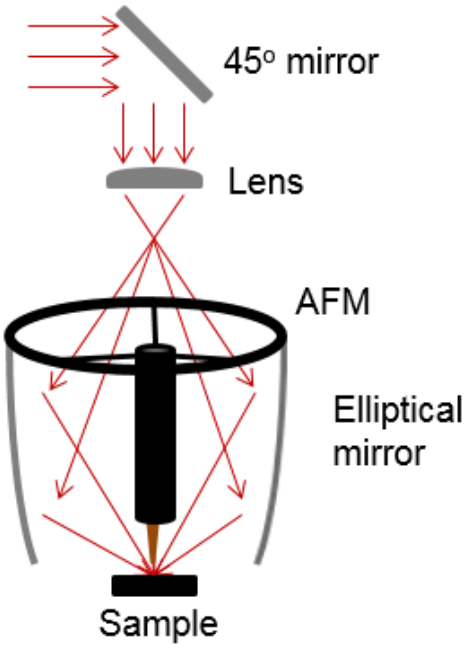

Figure 4.1: S-SNOM setup and light path; light is focused around the AFM and to the sample surface, scattered light is then recollected along the same paths

The incident light is focused by a lens through the top focal point of an elliptical mirror above the AFM. Approximately half of the light is blocked by the top of the AFM which is positioned down the vertical axis of the elliptical mirror. The other half passes around the AFM to the elliptical mirror which focuses the light to the tip and sample surface interaction point. Only 180^0 of the light from the elliptical mirror reaches the tip due to the tip protruding out one side of the AFM body. The size of the AFM components is clearly important to allow as much light as possible to reach the tip and sample surface interaction point. The interferometer detection style of this AFM is an advantage because the photodetector can be placed outside the apparatus rather than being another component to block light. Light scattered from the tip and sample surface interaction point is collected by the elliptical mirror and sent back out of the system

along one of the incident light paths where it can be detected in the far-field. Most s-SNOM setups developed to this point use a more direct focusing approach. A lens or off axis parabolic mirror will be positioned to one side of the AFM and the light will directly focus to the tip. The disadvantage of this approach is that scattered light can only be collected in the direction back to the focusing element. With the described elliptical mirror setup, scattered light is collected for approximately 180^0 radially around the tip.

The cantilever tip has two functions. The first is to confine and scatter incident light acting as an optical antenna. The second function is to concentrate the electromagnetic field at the tip apex to probe optical properties of a sample surface within the near-field distance of the field [25]. The light is confined to the size of the tip apex within the near-field distance, distance << λ, making the lateral resolution of the system the radius of curvature of the tip apex. This resolution depends on the tip itself, which is typically around 30 nm. A huge advantage of this field confinement is that it is wavelength independent [1]. Mid-infrared light approximately 11 μm provides vibrational finger prints of many materials. Optical experiments will typically only have spatial resolution around 5-6 μm with this wavelength due to diffraction limits so this field confinement improves spatial resolution in mid-infrared experiments by approximately 200 times. The field confinement in an s-SNOM system is shown in figure 4.2a and the field distribution at the cantilever tip for 632 nm light that is radially polarized in figure 4.2b.

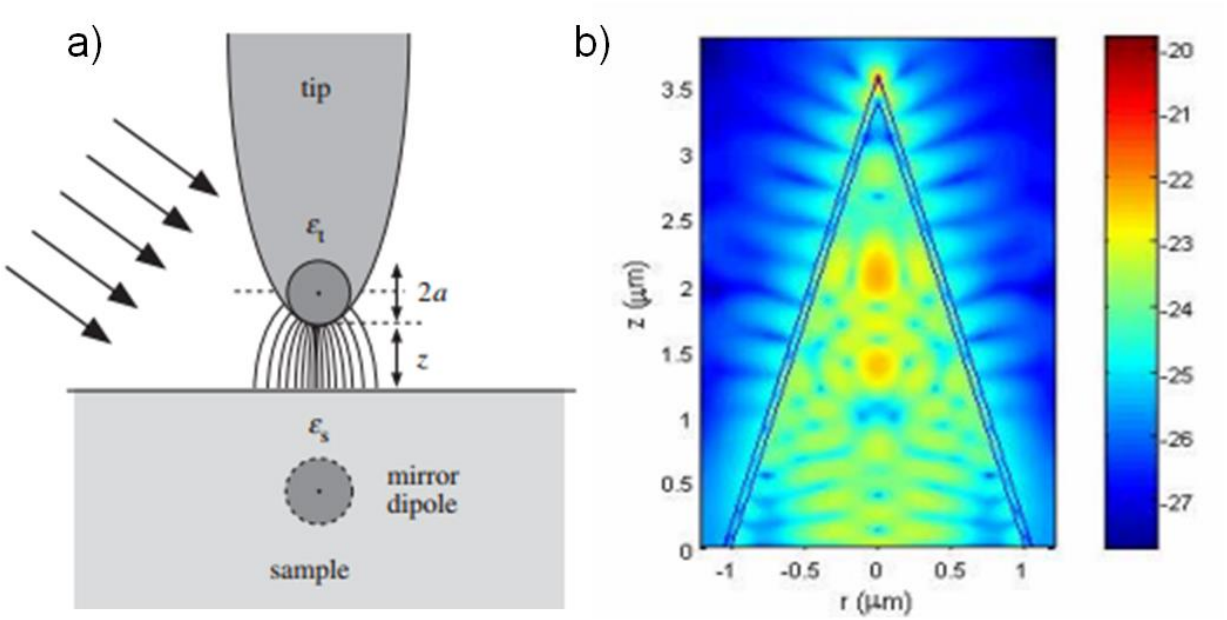

Figure 4.2: a) Field confinement in an s-SNOM system; incident light is confined to a sharp, probing tip close to sample surface in the near-field region (z << λ) [26] b) Model of EM field distribution intensity at tip apex for radially polarized light [27]

4.1.1. Finite Dipole Model

Thus far it has been discussed that in an s-SNOM system light can break the diffraction limit, but not what measurements are actually being taken. Light being scattered from the tip is the detected light, carrying information about the sample. This section will discuss how the near-field interaction takes place between the tip and sample surface, and what information can be gained from this.

Incident light focused onto the metallic tip causes it to become polarized. Early attempts to model the near-field interaction between the tip and sample surface approximated the tip as a single point dipole at the tip apex. This model is known as the point dipole model. It provided a qualitative picture of the near-field interaction, but

quantitatively did not match the material contrast experimentally obtained for different materials. In 2007, a new model by A. Cvitkovic, N. Ocelic and R. Hillenbrand based on the tip interacting with the sample as a monopole showed much better agreement with experiments [28]. This model is known as the finite dipole model and will be the focus of this section for explaining how interaction between the tip and sample surface occurs.

The finite dipole model assumes the shape of the tip to be a spheroid much smaller than the wavelength of light. A uniform field, E_0, is incident and normal to the sample surface. Figure 4.3 depicts the setup of the finite dipole model and the point dipole model.

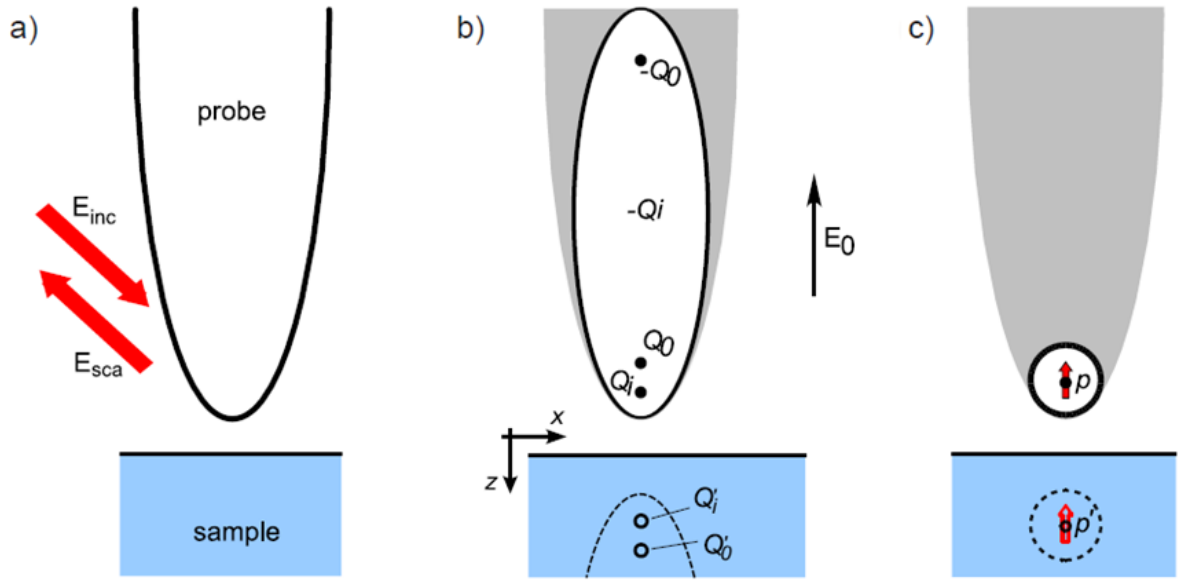

Figure 4.3: a) Tip is illuminated by incident field and then scatters a field in response b) Finite dipole model: Tip modeled as a spheroid that is polarized by incident field c) Point dipole model: Tip modeled as a point dipole at tip apex [28]

The incident field will polarize the tip and the induced charges will be what interact with the sample surface. The question is where the charges will orient

themselves. The entire spheroid will not interact with the sample surface within the near-field distance of a few nanometers so it needs to be known where charges will be located within the spheroid. The field given off by a conducting spheroid, E_s, is well known from electrostatic calculations to be [28]:

$$E_s(D) = \frac{\frac{2F(L+D)}{D^2 + L(2D+R)} + \ln[\frac{L-F+D}{L+F+D}]}{\frac{2F(L-\mathcal{E}_t R)}{LR(\mathcal{E}_t - 1)} - \ln[\frac{L-F}{L+F}]} E_0 \qquad (4.1.1)$$

Where:

D = distance from apex along z axis (major axis of spheroid)

L = distance from the center of spheroid to the apex

F = half the distance between the two foci of the spheroid

R = radius of curvature at the apex

$\mathcal{E}_t$ = dielectric function of the tip material

Knowing the electric field of the spheroid, A. Cvitkovic, N. Ocelic and R. Hillenbrand were able to try and find a charge distribution that would have a matching electric field. They found that the electric field close to the apex of the spheroid closely resembles that of a monopole.

$$E_m(D) = \frac{1}{(R+D)^2} \qquad (4.1.2)$$

Figure 4.4 shows these electric fields plotted vs. distance, along with some other candidates for likely charge distributions.

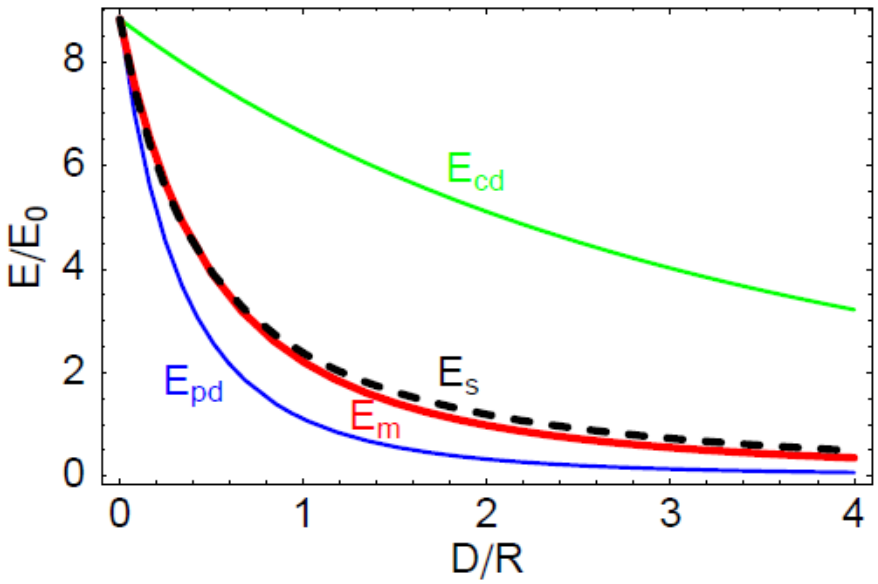

Figure 4.4: Electric field vs. distance along the z axis with spheroid parameters R= 0.1L and $\varepsilon_t = \infty$ (perfectly conducting). E_s (dashed black line) exact solution of spheroid, E_m (solid red line) field of a monopole at center of apex curvature, E_{pd} (solid blue line) field of a point dipole at spheroid apex, E_{cd} (solid green line) field of a point dipole at the center of the spheroid [28]

Figure 4.4 shows that the field of a monopole at the center of the apex curvature is a much better approximation than the field of a point dipole as in the point dipole model. From here on out the tip when illuminated with an incident field will be modeled as a spheroid with charge Q_0 at the center of the apex curvature and $-Q_0$ at the opposite position of the spheroid to maintain charge neutrality as depicted in figure 4.3b.

Near-field interaction will be due to charge Q_0. $-Q_0$ is too far from the sample surface to have a near-field effect. The total field outside of the spheroid will be both the incident field, E_0, and the field from the polarized spheroid, E_s, giving a field equation:

$$E(D) = E_0 + E_s(D) \qquad (4.1.3)$$

The effect of Q_0 on the sample surface can be thought of as an electrostatic method of images problem. It will induce charge Q_0' in the sample having charge [28]:

$$Q_0' = -\beta Q_0 \qquad (4.1.4)$$

$$\beta = \frac{\varepsilon_s - 1}{\varepsilon_s + 1} \qquad (4.1.5)$$

Where:

β = electrostatic reflection factor

ε_s = dielectric function of the sample

Q_0' will then act back on the spheroid again inducing further polarization. Similar to calculating the monopole approximation for the polarization from the initial incident field, the effect of the image charge on the spheroid needs to be calculated. It will create another charge distribution within the spheroid and the magnitudes and positions of the charge distributions need to be quantified to later calculate the actual interaction between the tip and sample. If the spheroid is grounded the total induced charge, Q_t, due to an external point charge, Q_e, is [29]:

$$Q_t = -Q_e \frac{\ln\left[\frac{L+F+D}{L-F+D}\right]}{\ln\left[\frac{L+F}{L-F}\right]} \qquad (4.1.6)$$

Then the distribution of Q_t needs to be known to approximate how much of it is involved in the near-field interaction. It has been shown that Q_t is actually the same as a

line charge distribution, q_i, along the major axis of the spheroid between the two foci. This line charge distribution is calculated to be [30]:

$$q_i(z) = \frac{-Q_e \Theta(F^2 - z^2)}{2F} \sum_{n=0}^{\infty} (2n+1) \frac{Q_n\left[\frac{L+D}{F}\right] P_n\left[\frac{L}{F}\right] P_n\left[\frac{z}{F}\right]}{Q_n\left[\frac{L}{F}\right]} \qquad (4.1.7)$$

Where:

Θ = unit step function

Q_n = n-th order Legendre function of the 2nd kind

P_n = Legendre polynomials

A representation of the line charge distribution within the grounded spheroid due to external charge, Q_e, is shown in figure 4.5.

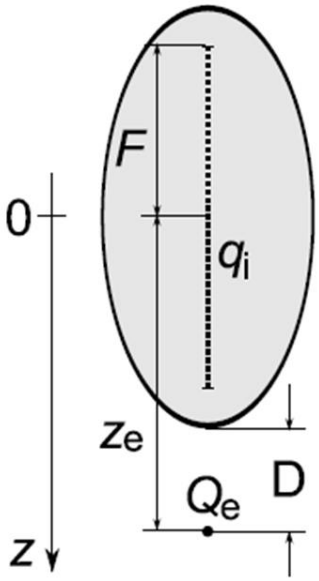

Figure 4.5: Charge distribution, q_i, in grounded spheroid due to external charge Q_e [28]

The highest density of charge within q_i is located at the spheroid foci. Therefore this charge distribution will be modeled as a point charge, Q_i, located at the spheroid focus as shown in figure 4.3b. Not all of the charge distribution, q_i, will contribute to the near-field interaction so Q_i will only contain part of this charge [28]:

$$Q_i = gQ_t = \int_{L-(R+D)}^{L} q_i(z)dz \qquad (4.1.8)$$

This has been the case of a grounded spheroid where negative charge has been able to leave the system. When the spheroid is not grounded the induced charge will orient itself to maintain the spheroid surface at equipotential. Equation 4.1.8 is modified by the addition of a negative charge to maintain charge neutrality and turns into [28]:

$$Q_i = g'Q_t = \left(g - \frac{R+D}{2L}\right)Q_t \qquad (4.1.9)$$

At this point in the model, there are two induced charges, Q_0 and Q_i, in the spheroid taking part in the near-field interaction. Also there are two image charges, Q_0' and Q_i', in the sample surface taking part in the interaction. This is shown in figure 4.6.

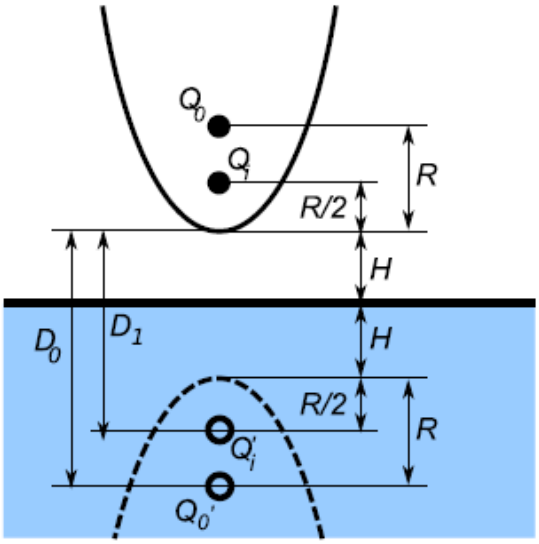

Figure 4.6: Schematic of induced charges taking part in the near-field interaction between tip and sample surface [28]

The distances of the two image charges from the spheroid apex can be read from figure 4.6 as:

$$D_0 = 2H + R \qquad (4.1.10)$$

$$D_1 = 2H + \frac{R}{2} \qquad (4.1.11)$$

The next step is to find the relationship between the monopole charges in the spheroid and the image charges. This is done by combining equations 4.1.6, 4.1.9, 4.1.10, and 4.1.11. The result after putting these equations together is as follows:

$$Q_0 = f_0 Q_0{}' = -Q_0{}' \left(g - \frac{R+H}{L}\right) \frac{\ln\left[\frac{4L}{4H+3R}\right]}{\ln\left[\frac{4L}{R}\right]} \qquad (4.1.12)$$

$$Q_i = f_1 Q_i{}' = -Q_i{}' \left(g - \frac{3R + 4H}{4L} \right) \frac{\ln\left[\frac{2L}{2H + R}\right]}{\ln\left[\frac{4L}{R}\right]} \qquad (4.1.13)$$

It was stated earlier in equation 4.1.4 that the image charges are related to the monopole charges in the spheroid by the electrostatic reflection factor. Now there are two different relations between the tip and surface charges. They can be used in combination to relate the induced charges within the spheroid independent of the image charges. This relation comes out to be:

$$Q_i = \frac{-\beta f_0}{1 + \beta f_1} Q_0 \qquad (4.1.14)$$

This gives the main point of this model, a relationship between Q_i and Q_0. Q_0 was induced by the incident light. Then Q_i was induced by the sample itself. This is the near-field interaction. The near-field contrast factor between the tip and sample can be written as:

$$\eta = \frac{Q_i}{Q_0} = \frac{\beta \left(g - \frac{R + H}{L} \right) \ln[\frac{4L}{4H + 3R}]}{\ln\left[\frac{4L}{R}\right] - \beta \left(g - \frac{3R + 4H}{4L} \right) \ln[\frac{2L}{2H + R}]} \qquad (4.1.15)$$

There is a clear near-field interaction taking place between the tip and sample surface. The next question to be answered is how does it get detected and measured experimentally. The scattered light from the tip is the quantity being measured at the detector. The tip has essentially become a radiating dipole, $E_{sca} \sim p = \alpha E_0$, where p is the dipole moment and α is the dipole polarizability. The dipole moment consists of two parts in the same way that there are two sets of charges for the near-field interaction, $p_{eff} = p_0 + p_i$. The general definition for a simple dipole moment is p=q*d. At this point the

positions and charge magnitudes are known for this scenario and can be used to find the tip polarizability for the monopole approximation of the charges [28]:

$$p_0 = 2LQ_0 \qquad (4.1.16)$$

$$p_i = \eta LQ_0 \qquad (4.1.17)$$

$$Q_0 = R^2 E_s(0) \qquad (4.1.18)$$

$$\alpha_{eff} = \frac{p_{eff}}{E_0} = R^2 L \frac{\frac{2L}{R} + \ln\left[\frac{R}{4eL}\right]}{\ln\left[\frac{4L}{e^2}\right]} \left(2 + \frac{\beta\left(g - \frac{R+H}{L}\right)\ln[\frac{4L}{4H+3R}]}{\ln\left[\frac{4L}{R}\right] - \beta\left(g - \frac{3R+4H}{4L}\right)\ln[\frac{2L}{2H+R}]} \right) \qquad (4.1.19)$$

With the polarizability now known, it is time to calculate the actual scattered field. However, one more factor that needs to be accounted for is the incident light is focused onto the tip directly as well as reflects from the surface and interacts with the tip post reflection as well. This can be accounted for with the Fresnel reflection coefficient pertaining to p-polarized light [28]:

$$E_{sca} \propto \left(1 + {r_p}^2\right)^2 \alpha_{eff} E_{inc} \qquad (4.1.20)$$

Now there is a measure of how the scattered light will be affected by the near-field interaction. Quantities such as R and H can be measured experimentally within the system. Even a good estimate for L can be obtained by knowing the size of the actual cantilever tip being used as long as it is much smaller than the wavelength of the incident light. g is a factor that needs to be parameterized to fit experimental data. A reasonable estimate is g=0.7. Thus the change in contrast when running s-SNOM experiments comes from β which is a quantity based on the dielectric function of the

sample. S-SNOM measures the contrast between different materials based on their dielectric properties.

Cvitkovic, Ocelic and Hillenbrand tested their finite dipole model vs. the point dipole model by comparing the results of the models to actual experimental data. They used a very similar s-SNOM system to the one described in this thesis and use a mid-infrared light source. They plot the amplitude of the near-field signal as the tip is brought closer and closer to an Au surface. Their results are shown in figure 4.7.

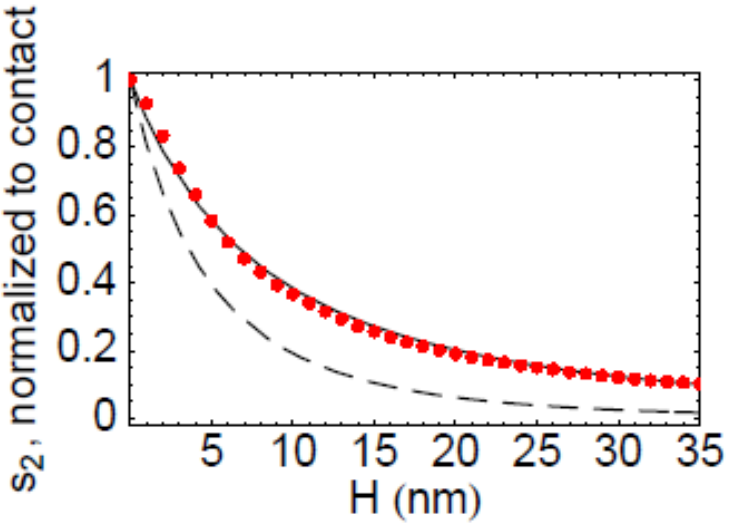

Figure 4.7: Approach curves for the near-field signal as the tip is brought into contact with an Au surface normalized to the value at H=0. Experimental data (red dots), finite dipole model (solid black line), point dipole model (dashed black line) [28]

It can be seen from figure 4.7 that the finite dipole model is in great agreement with the actual experimental data. The formerly accepted point dipole model does provide the correct trend, but is not an accurate quantitative calculation.

The finite dipole model can even predict near-field contrast due to phonon enhancement which is also shown by Cvitkovic, Ocelic and Hillenbrand. Equation 4.5 predicts that as the real part of the dielectric function of a material approaches -1, β will increase rapidly as long as the imaginary part of the dielectric function remains small. This is the case for 4H-SiC in the mid-infrared regime, it has a phonon-polariton resonance [31]. A thin Au film was placed on part of a 4H-SiC sample for normalizing the signal and seeing the contrast between the two different materials at various light frequencies. The enhancement due to the phonon resonance in 4H-SiC is shown in figure 4.8.

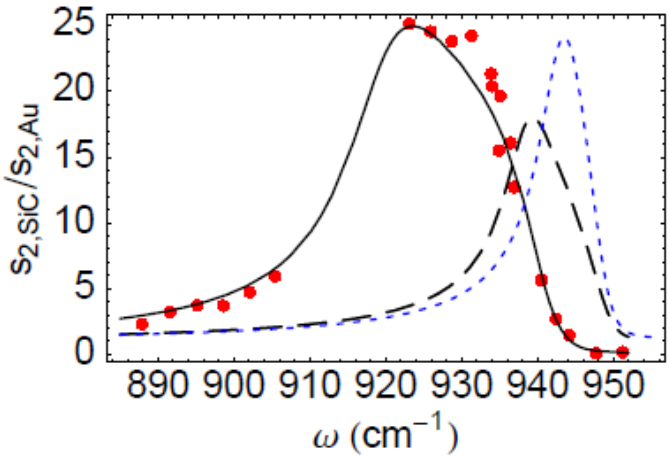

Figure 4.8: Near-field signal amplitude contrast between 4H-SiC and Au at different frequencies of incident light. Experimental data (red dots), finite dipole model prediction (solid black line), point dipole model prediction (dashed black line), and point dipole model with adjusted fitting parameters (dashed blue line) [28]

Figure 4.8 clearly shows a near-field signal enhancement in 4H-SiC due to a phonon resonance. The finite dipole model is once again in great agreement with experimental data whereas the point dipole model is not in quantitative agreement. This

figure shows the potential of s-SNOM as a spectroscopic tool. It provides sub-diffraction limit resolution for obtaining optical fingerprints of the dielectric properties of materials.

4.1.2. Pseudoheterodyne Detection

Another piece of this s-SNOM system necessary to discuss is the detection scheme. The light is being scattered off the tip and contains information about the near-field interaction. However, the light reaching the detector also contains unwanted background contributions that can produce artifacts in raster scan images that are being created. This section will discuss a pseudoheterodyne detection scheme implemented to distinguish the desired near-field signal from any unwanted background signal reaching the detector.

The light being focused to the tip and sample interaction area is much larger in size than the tip itself. Therefore there will be light that reflects off various other objects such as the rest of the cantilever and directly off the sample surface. S-SNOM is run in non-contact mode imaging so the tip is actually oscillating above the sample surface at frequency, Ω. It typically has an oscillation amplitude of a few tens of nanometers. Within this distance variation, the near-field signal is constantly changing as the tip oscillates due to the evanescent nature of the near-field interaction. The near-field signal has a nonlinear distance dependence. The near-field signal can be demodulated at higher harmonics due to its nonlinear dependence on the distance from the sample surface. However the background signal is not evanescent and is essentially a constant within the near-field approximation [32]. Therefore the background signal will have minimal contribution at higher harmonics. By demodulating at higher harmonics

measurements of the gradient with respect to the distance are being taken. The background signal is constant and doesn't have this gradient. Figure 4.9 shows near-field amplitude scan images demodulated at different harmonics, nΩ, of the tapping frequency, Ω = 72 kHz, with incident light of 10.8 μm. These images were taken with this specific s-SNOM system and are of an Au electrode on LAO/STO.

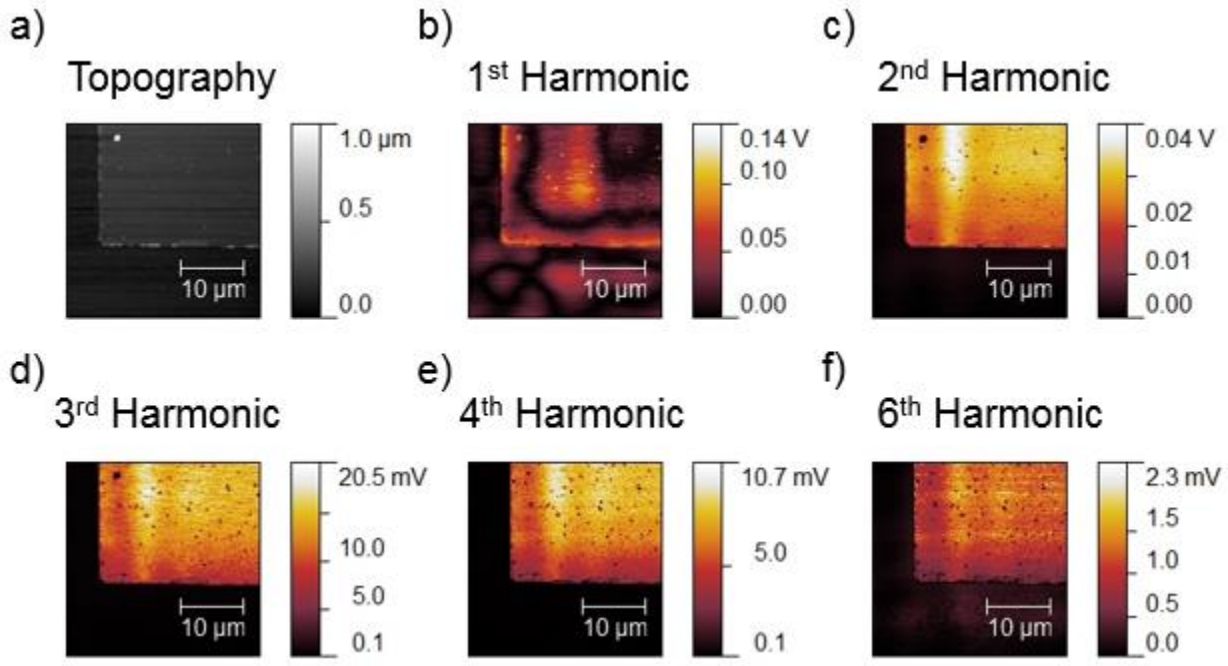

Figure 4.9: Near-field amplitude images of an Au electrode on LAO/STO with 10.8 μm wavelength at different demodulation harmonics. a) Topography of area scanned b) 1st harmonic c) 2nd harmonic d) 3rd harmonic e) 4th harmonic f) 6th harmonic

Demodulation at the first harmonic shows contrast in areas that are of one constant material. This is due to background signal contribution. The 2nd harmonic and higher shows much clearer imaging because of suppression of the background signal. The contrast within the Au electrode is due to surface plasmon resonances that will be discussed in section 4.2. Also defects can attribute to contrast, but these are not

artifacts of unwanted signal. Once reaching much higher harmonics such as the 6th harmonic shown, the image starts to become noisy due to a low signal to noise ratio thus there is a limit to how high a harmonic can be used for demodulation. However, just going to the 2nd harmonic suppresses most background contributions.

Demodulating at higher harmonics is the first essential step for background suppression, but it does not get rid of the entire background effect. The background signal couples to the varying near-field signal as will be shown in this section. First the scattered electric field, E_s, being collected can be written as a Fourier series [32]:

$$E_s = \sum_n \tau_n \, e^{in\Omega t} \qquad (4.1.21)$$

The entire field is composed of two parts, the desired near-field signal and the background signal. Therefore there are two coefficients in the Fourier series:

$$\tau_n = \sigma_n + \sigma_{b,n} \qquad (4.1.22)$$

Where:

σ_n = nth coefficient of the near field signal

$\sigma_{b,n}$ = nth coefficient of the background signal

As already described, the background signal is nearly all in the 1st harmonic. $\sigma_{b,n}$ will be treated as a constant $\sigma_{b,0}$. The output voltage of the detector is always proportional to the square of the field, u α $|E_s|^2$. This gives the output voltage of the detector as [32]:

$$u \approx \kappa\left(\sigma_{b,0}\sigma_n{}^* + \sigma_{b,0}{}^*\sigma_n\right) = 2\kappa s_{b,0}s_n \cos\left(\phi_{b,0} - \phi_n\right) \qquad (4.1.23)$$

Where:

u = detector output voltage

$\sigma = s\, e^{i\phi}$

s = amplitude of σ

ϕ = phase of σ

κ = proportionality constant for the sensitivity of the detector

Equation 4.1.23 shows the coupling of the background signal to the near-field signal. Even at higher harmonics where the background signal itself is suppressed directly, it still has an effect on the near-field signal. The point of the pseudoheterodyne detection being worked through is to alleviate the interference between the two signals.

In chapter two the optical setup of this s-SNOM setup was discussed. When the light first reaches the beamsplitter, one half of the light, the main arm, continued to the tip and sample, and the other half of the light was not discussed. The second half of the light which will be known as the reference arm is what is used for the pseudoheterodyne detection scheme. The reference arm is directed to travel parallel to the main arm and at the same height, but offset by 17 mm. The two arms then travel to identical optical elements up to the high vacuum chamber. In the high vacuum chamber, the main arm hits a 45 degree mirror that directs the arm down towards the sample. At this point, the

reference arm retroreflects off a separate planar mirror that is 17 mm offset from the 45 degree mirror. When the reference arm is being offset from the main arm, one mirror it reflects off of is a vibrating mirror. It is made to oscillate with frequency, M, by a piezoelectric actuator. The vibrating mirror allows for phase modulation of the reference arm. The field of the oscillating reference arm is a Fourier series [1, 33]:

$$E_R = \sum_m \rho_m(\gamma) e^{i\gamma sin(Mt)} \qquad (4.1.24)$$

Where:

M = frequency of oscillating mirror

γ = modulation depth

ρ_m = amplitude coefficient of reference wave

When both arms reach the beamsplitter in the return path of the light, they interfere on their way to the detector. This interference can be handled in the same manner as the interference between the near-field signal and the background signal [33]:

$$u \approx |(\sigma_n + \sigma_{b,n}) e^{in\Omega t} + \rho_m(\gamma) e^{i\gamma \sin(Mt)}|^2 \qquad (4.1.25)$$

Equation 4.1.25 creates signals at multiple frequencies, nΩ, mM, and nΩ ± mM. The signal at mM is purely due to the reference arm. The nΩ signals are still a combination of the interfering near-field signal and background signal. The most useful signal is the nΩ ± mM. It contains two terms, the reference arm interfering with the near-field signal and the reference arm interfering with the background signal. However, at these sideband frequencies the near-field signal and background signal are not coupled to

each other. They are two separate signals at the same frequency. This can be combined with demodulating at the higher harmonics. At higher harmonics the background signal is very weak. Thus the signal at nΩ ± mM is dominated by the near field signal for n>1. M needs to be shifted from the tapping frequency of the cantilever, Ω. If they are close in value or multiples of each other, the different frequencies of signals can end up being the same frequency. Typical values used in this specific s-SNOM system are Ω = 72 kHz and M = 200 Hz. Figure 4.10 depicts the signals being separated into sidebands containing pure near-field signal.

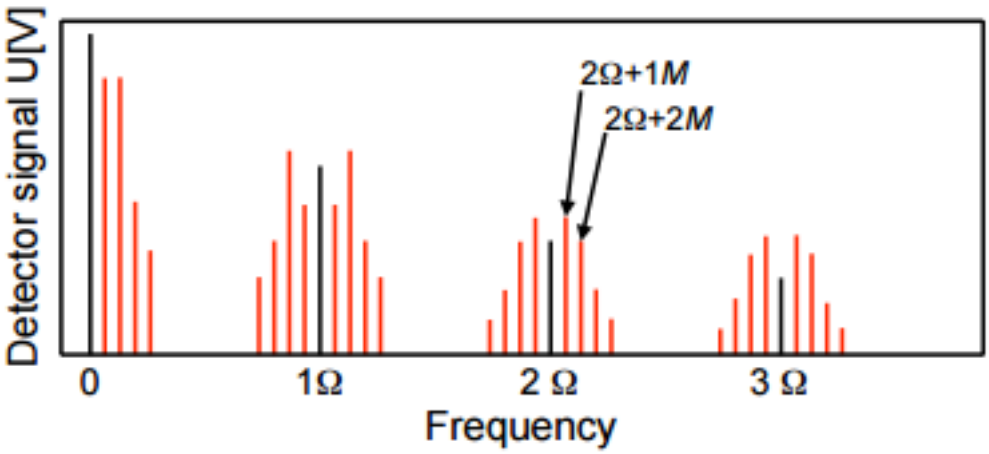

Figure 4.10: Demodulation frequencies being detected. Red lines contain pure near-field signal information. Overall enhancement of signal is due to amplitude increase from interference with the reference arm. [33]

The pseudoheterodyne detection scheme combined with higher harmonic demodulation allows for a background free near-field signal to be acquired. Demodulating at the sidebands nΩ ± mM allows for accurate amplitude and phase images to be acquired through a lock-in amplifier. Also interference with a high intensity

reference arm can increase the overall signal to noise ratio of the entire system by increasing the amplitude of the overall signal. Figure 4.11 shows near-field scans taken with and without the pseudoheterodyne detection scheme of an Au electrode on LAO/STO. Both are taken at the 2nd harmonic of the tapping frequency. There is minimal difference between the images. The phase is more reliable with the pseudoheterodyne detection scheme being used however. Any change in the background signal during the scanning process would show up on the scans without the pseudoheterodyne detection scheme. These scans can easily take up to an hour of time to complete so it is important to alleviate the possibility of background fluxuations in the final images.

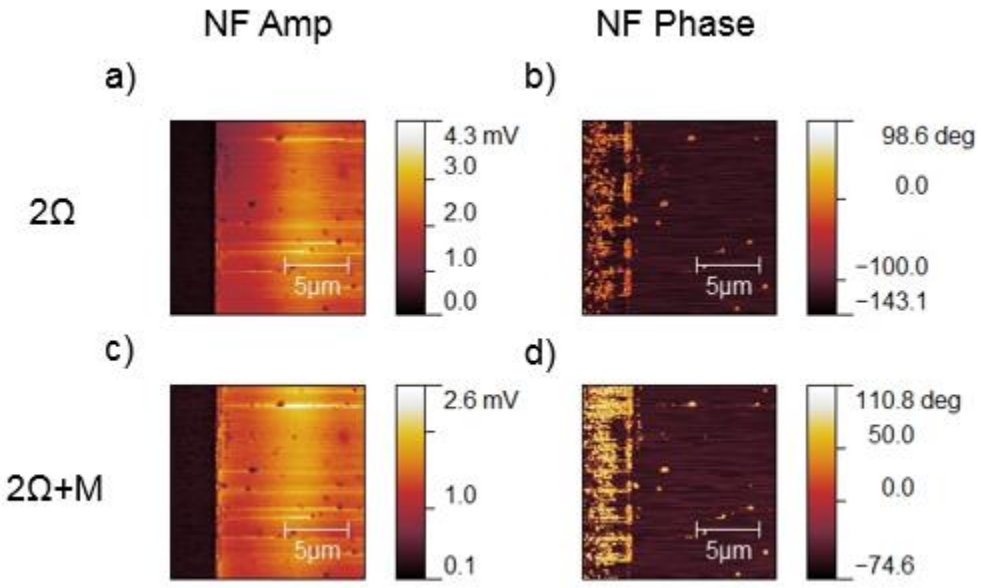

Figure 4.11: Au electrode on LAO/STO a), b) near-field images of amplitude and phase demodulated at 2Ω c), d) near-field images of amplitude and phase demodulated at 2Ω+1M; Ω ≈ 72 kHz, M = 200 Hz

4.2. Au Surface Plasmon

This section will demonstrate this s-SNOM systems capability. It will show results of inducing and imaging surface plasmons at an Au and air interface. It will go through the theory behind surface plasmons, and then show images acquired with this s-SNOM system.

Plasmons are a collective oscillation of free electrons in a metal induced by photons [34]. When these oscillations of electrons are on the surface of the metal then they can be termed surface plasmons. These surface plasmons are a major area of research currently in the world of nanophotonics. The beauty of surface plasmons is ability to propagate light across a metal surface on a subwavelength scale. They can be used as nanocircuit waveguides in the further development of nanotechnology [34]. Surface plasmon resonances can be used in many applications. Solar cells use surface plasmons to increase the number of excited charge carrier from the incident light. They not only can guide light to specific absorbing layers of the solar cell, but also increase the overall absorption by confining the light to the solar cell surface for a longer duration of time [35]. Surface plasmons resonances are created for specific frequencies of incident photons and have characteristics from that frequency. They can also be used as a sensing application to identify a molecular structure [35].

The mathematical treatment to identify a solution of an electromagnetic surface oscillation can come straight from a classical treatment of Maxwell's equations. Start by considering the nonmagnetic interface between a metal and dielectric medium at $z = 0$.

Within the mathematical treatment it will be shown why the two mediums are a metal and dielectric. Maxwell's equations without any external charges are written as:

$$\nabla \times H_i = \frac{\varepsilon_i}{c}\frac{\partial E_i}{\partial t} \qquad (4.2.1)$$

$$\nabla \times E_i = -\frac{1}{c}\frac{\partial H_i}{\partial t} \qquad (4.2.2)$$

$$\nabla \cdot H_i = 0 \qquad (4.2.3)$$

$$\nabla \cdot (\varepsilon_i E_i) = 0 \qquad (4.2.4)$$

Where:

i = 1 or 2; 1 for the metal medium z < 0, 2 for the dielectric medium z > 0

H = magnetic field

E = electric field

c = speed of light

Ɛ = frequency dependent dielectric function

The goal is to induce an oscillation of electrons along the interface. Therefore the incident light must be p-polarized to have an electric field component normal to the interface [36]. With this in mind, the fields of the incident light traveling from the dielectric to the interface can be written as [36]:

$$E_i = (E_{ix}, 0, E_{iz})e^{-\kappa_i|z|}e^{i(q_i x-\omega t)} \qquad (4.2.5)$$

$$H_i = \big(0, H_{iy}, 0\big)e^{-\kappa_i|z|}e^{i(q_i x-\omega t)} \qquad (4.2.6)$$

Where:

κ = evanescent decay constant

q = wave vector

ω = angular frequency

x = propagation direction

Next input equations 4.2.5 and 4.2.6 into Maxwell's equations. This finds a relation between the electric and magnetic fields and between the dielectric functions and wave vectors:

$$i\kappa_1 H_{1y} = \frac{\omega}{c}\varepsilon_1 E_{1x} \qquad (4.2.7)$$

$$i\kappa_2 H_{2y} = -\frac{\omega}{c}\varepsilon_2 E_{2x} \qquad (4.2.8)$$

$$\kappa_i = \sqrt{{q_i}^2 - \varepsilon_i(\frac{\omega}{c})^2} \qquad (4.2.9)$$

Boundary conditions for Maxwell's equations state that both fields must be continuous for their components parallel to the surface [37]. Then by using these boundary conditions for equations 4.2.7 and 4.2.8, two conditions are found:

$$H_{1y} = H_{2y} \qquad (4.2.10)$$

$$\frac{\kappa_1}{\varepsilon_1} H_{1y} + \frac{\kappa_2}{\varepsilon_2} H_{2y} = 0 \qquad (4.2.11)$$

These two conditions are both met for only one scenario. This scenario is known as the surface plasmon condition [36]:

$$\frac{\varepsilon_1}{\kappa_1} + \frac{\varepsilon_2}{\kappa_2} = 0 \qquad (4.2.12)$$

This surface plasmon condition is why the two mediums are a metal and dielectric. One of the dielectric functions of the two mediums needs to be negative at a certain frequency. This can be the case for many metals [38].

Boundary conditions also apply to the wave vector itself. The wave vector must be continuous across the surface such that $q = q_1 = q_2$. By combining this with equation 4.2.12 (the surface plasmon condition) and equation 4.2.9, a dispersion relation for the surface plasmon can be obtained:

$$q(\omega) = \frac{\omega}{c} \sqrt{\frac{\varepsilon_1 \varepsilon_2}{\varepsilon_1 + \varepsilon_2}} \qquad (4.2.13)$$

In the experiment going to be demonstrated the dielectric medium is air. Therefore ε_2 can be set to 1. The next step is to figure out what the dielectric function of the metal can be expressed as. Starting from Newton's equation of motion in the Drude Model (free electron model), the conductivity of a metal can be written as [37]:

$$\sigma(\omega) = \frac{ne^2\tau}{m(1 - i\omega\tau)} \qquad (4.2.14)$$

Where:

n = electron density of the metal

τ = relaxation time

m = effective mass of the electron

Equation 4.2.14 commonly inserts the plasma frequency of the metal. The plasma frequency is the characteristic frequency of electrons about their equilibrium position when displaced by an electric field [39]. The plasma frequency is defined as equation 4.2.15 and inserting into equation 4.2.14 yields:

$$\omega_p = \sqrt{\frac{ne^2}{m\varepsilon_0}} \qquad (4.2.15)$$

$$\sigma(\omega) = \frac{\varepsilon_0 {\omega_p}^2 \tau}{1 - i\omega\tau} \qquad (4.2.16)$$

From this point, it is just a matter of shifting between the related quantities of σ to Ɛ. By doing this we can define a formula for the dielectric function of metal to use in the dispersion relation for a surface plasmon [37, 36]:

$$\sigma(\omega) = i\omega(\varepsilon_0 - \varepsilon) \qquad (4.2.17)$$

$$\varepsilon(\omega) = 1 - \frac{{\omega_p}^2}{\omega\left(\omega + \frac{i}{\tau}\right)} \qquad (4.2.18)$$

Now actual solutions to these equations will be shown for an Au and air interface. The relaxation time for Au is 92.6 fs, and the plasma frequency is $1.374*10^{16}$ / s [40]. Figure 4.12 shows the surface plasmon dispersion curve for an Au and air interface plotted using mathematica.

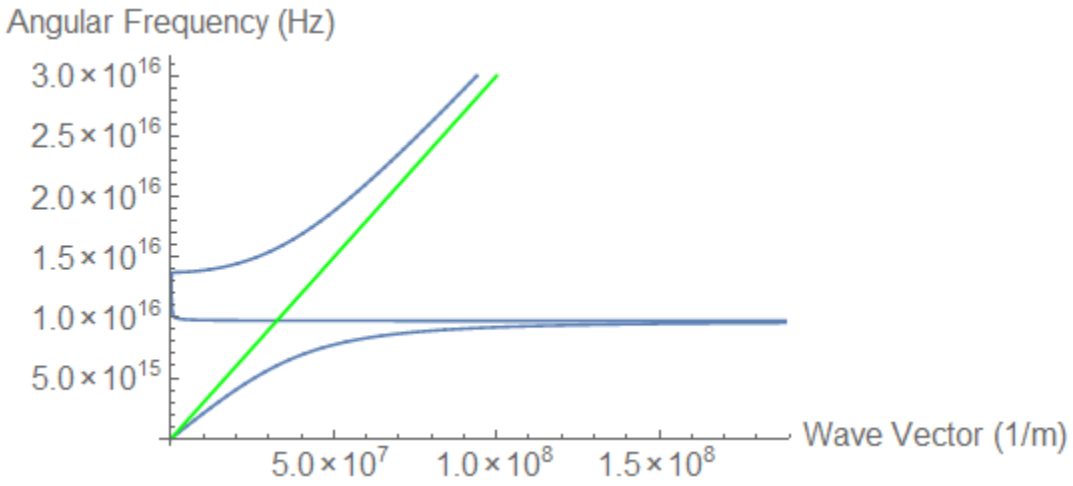

Figure 4.12: Blue line is the surface plasmon dispersion curve of Au and air interface. Green line represents dispersion of light in air ($q = \omega/c$)

As can be seen in figure 4.12, at very high and low frequencies the surface plasmon resembles light. At desired frequencies however the surface plasmon distinguishes itself and disperses throughout the interface as the photons are coupled to the electron oscillations. The dispersion curve tells for what frequencies, to look for a plasmon. The blue line residing at higher frequencies than the light in air is bulk plasmon resonances. S-SNOM is a surface scanning instrument and is concerned with surface plasmons. The blue line below the frequency of light is surface plasmon resonances. The real part of equation 4.2.13 gives the expected wavelength of the

surface plasmon resonance. In the case of this Au and air interface with incident light of 636 nm, the expected surface plasmon wavelength is 620 nm.

This Au and air interface surface plasmon was imaged in this s-SNOM system. As demonstrated earlier in this chapter, resonances within a material will provide a change in near-field signal contrast between materials. Figure 4.13 shows two surface plasmons imaged. The sample tested is 100 nm thick Au electrodes on LAO/STO in air.

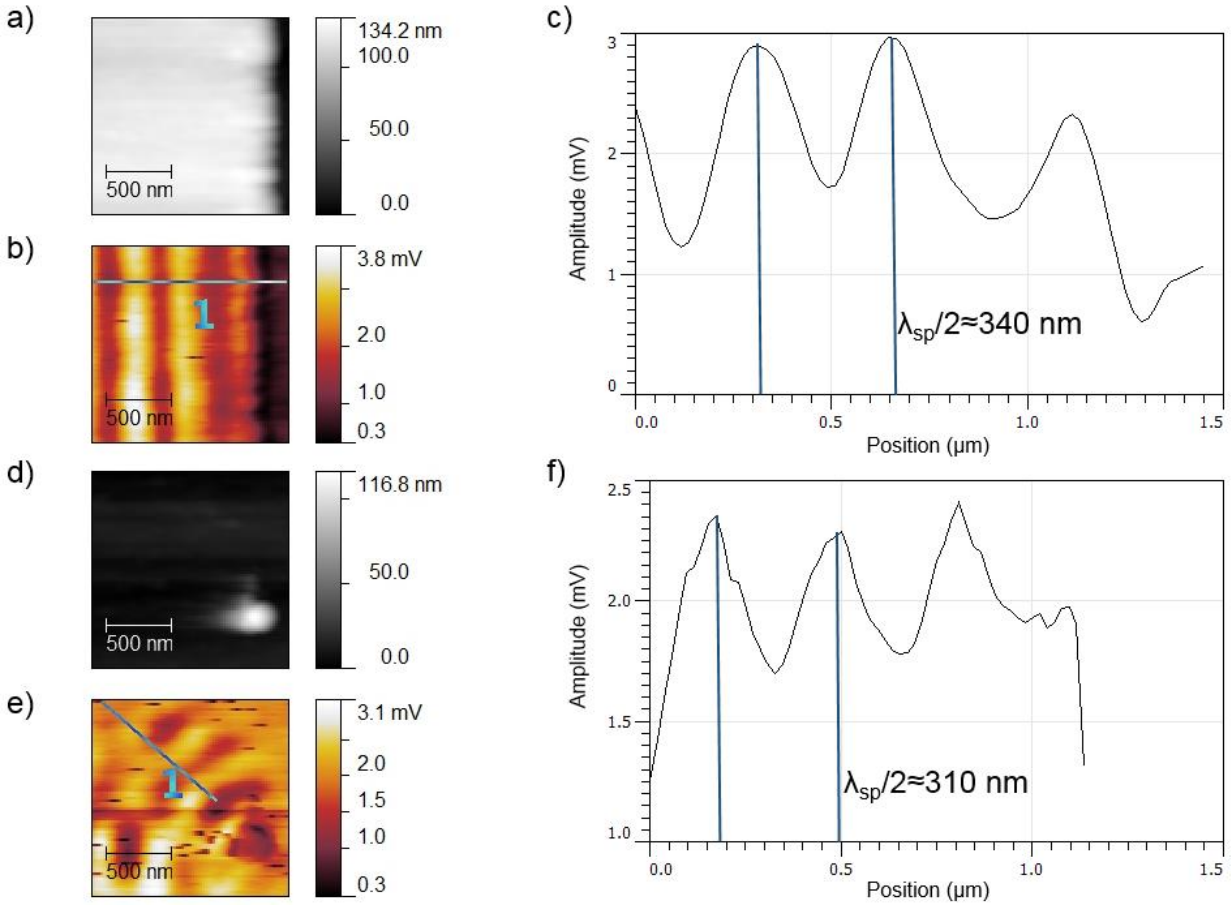

Figure 4.13: Scan images of Au electrodes on LAO/STO in air a) AFM topography of edge of electrode b) Near-field amplitude image of edge of electrode c) Cross section of line 1 image b d) AFM topography around defect on electrode e) Near-field image around defect on electrode f) Cross section of line 1 image e

During these scan images, surface plasmons are actually initiated at the position of the tip. This is where there is a strong confinement of the electric field at the tip apex. Defects and edges on the surface act as reflectors for the surface plasmon [41]. The fringes actually seen in near-field images are the interference pattern of the initial and reflected surface plasmon waves propagating. For that reason, the distance between fringes in the images corresponds to half the wavelength of the surface plasmon [41]. In figure 4.13 fringes are clearly noticeable coming from the edge of the electrode and a defect on the electrode in the near-field images. However, there is no fringe like pattern in the topography images. Therefore the fringes are an optical response of some kind, not a topography artifact. Theoretically, the fringe separation calculated in this section should be 310 nm. The fringe distances seen in the images are 340 nm and 310 nm, in good agreement with the theoretical value.

Surface plasmon imaging is one of the primary uses that s-SNOM systems have been used for to this point in time. Au is one of the most popular materials for seeing these surface plasmons because it can be done in the visible spectrum. These surface plasmon images demonstrate the successful design and construction of this s-SNOM system.

5. CURRENT AND FUTURE RESEARCH

This chapter will discuss two research projects that are already underway involving this s-SNOM system. The two projects involve two unique materials, InSe thin films and NbO_2. The progress and future intention of each project will be presented.

5.1. InSe Thin Film

Today's technology is based on silicon. The problem is that silicon technology has reached a limit in advancement. The world is searching for the next technological generation. Photovoltaics, converting light into electricity, is the one areas being researched currently [42]. Plasmonics are of particular interest within the field of photovoltaics [43]. Group III – VI compounds have been getting much interest due to their large photoresponse. This makes them great candidates for photovoltaic applications. Specifically InSe because the band structure of it's hexagonal lattice overlaps so well with the visible spectra [44].

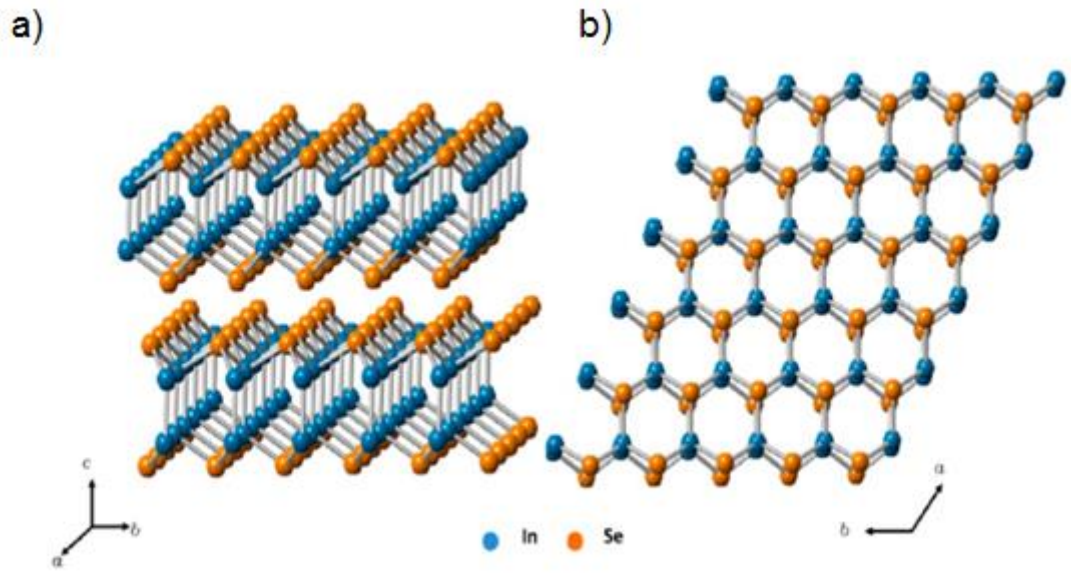

Figure 5.1: Crystal Structure of InSe [44]

InSe thin films have photoresponsivity of 34.7 mA/W with a response time of 488 µs [44]. The band gap of bulk InSe is 1.2 eV where as it increases to 1.4 eV for few layer thin films [44]. This thickness dependence even adds tunability to it's already great

photovoltaic advantages. However the question being propsed is what if suface plasmons can be induced on InSe thin films to further enhance and control these photovoltaic properties. InSe thin films do meet the criteria of having a negative dielectric function in the far infrared spectrum [45].

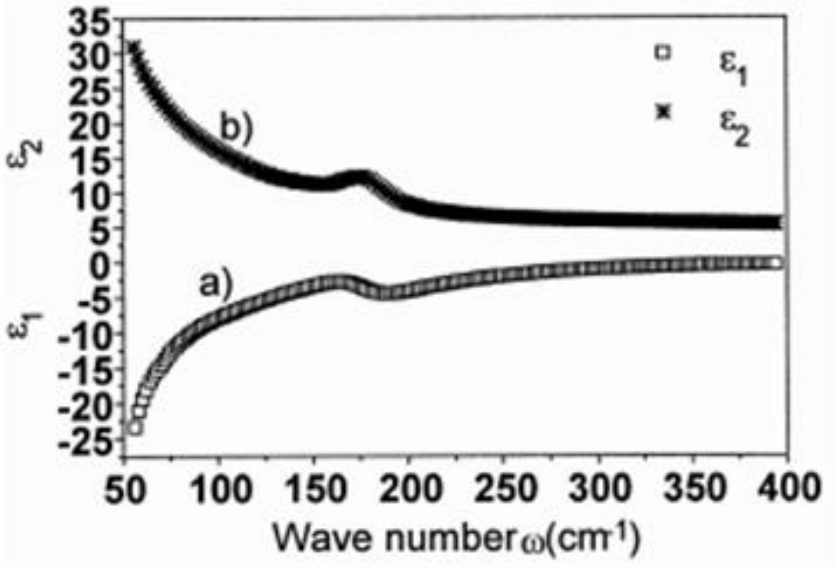

Figure 5.2: Theoretically calculated a) real and b) imaginary parts of the dielectric function of 800 nm thick InSe thin film [45]

The goal is to induce and image a surface plasmon on InSe thin film. It is tough to plot an accurate dispersion curve for InSe thin films because there is not much data on them to this point. Also the variables such as carrier concentration are going to vary greatly depending on the thickness and quality of the thin film. Figure 5.3 shows the estimated dispersion curve. The data used for the plot is incident light of 10.8 μm, n = $6.05*10^{17}$ cm^{-3}, $m_{eff} = 0.12\ m_0$, and $\tau = 15.7$ fs [45].

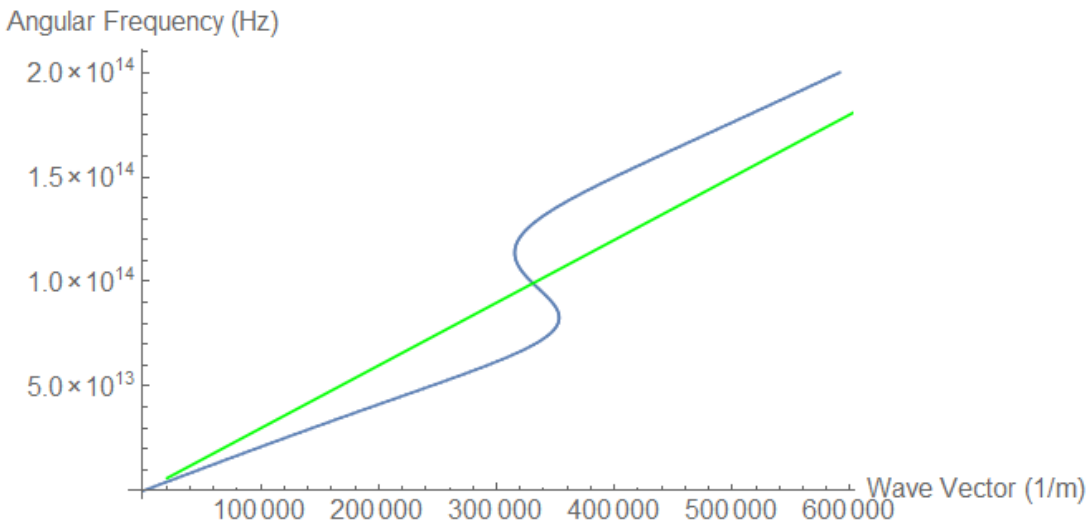

Figure 5.3: Dispersion curve for InSe film in air

The dispersion curve shows minimal momentum being transferred into the InSe thin film. Also at the wavelength of incident light being used, 10.8 µm or wave vector $5.8*10^5\ m^{-1}$, if a plasmon was to be induced it would more likely be a bulk plasmon. However, by increasing the carrier density of the InSe thin film, it becomes more condusive to a surface plasmon resonance at this wavelength. Also if the thin film is considered to be a two dimensional material, it is an entirely different model for the dispersion curve and must be plotted as:

$$\omega = \frac{\omega_p}{\sqrt{2}}(1 \pm e^{-|q|d})^{1/2} \qquad (5.1.1)$$

In this experiment the thickness of the film is d = 60 nm. Figure 5.4 shows the dispersion curve by increasing the carrier density by 100 times, and for treating the film as a two dimensional material.

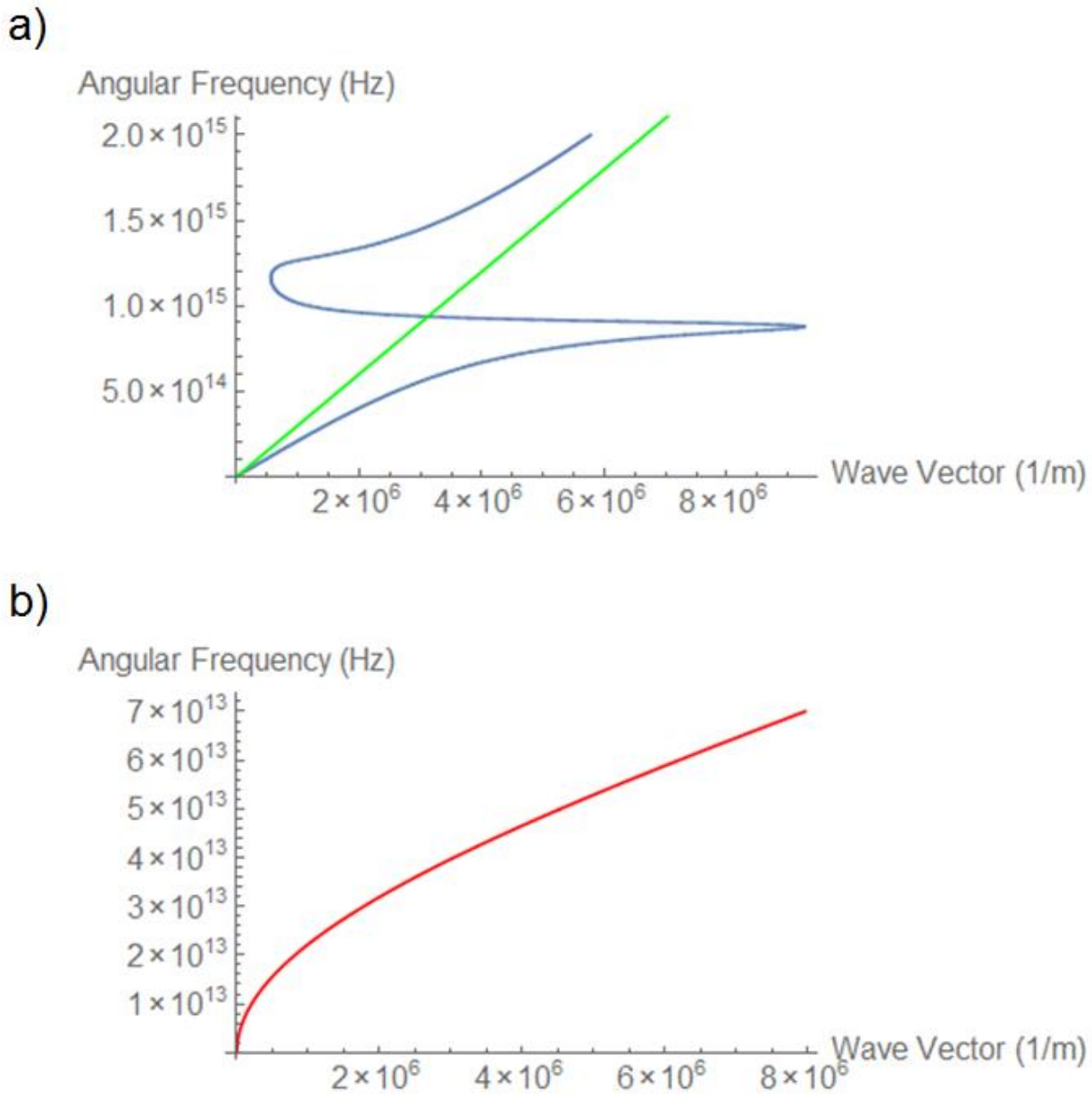

Figure 5.4: a) 3D dispersion curve of InSe film in air with carrier density increased by 100 times b) 2D dispersion curve with InSe film of 60 nm in air

InSe thin film samples on PMMA substrates are supplied by Dr. Xuan Gao at Case Western University. The sample being used for testing is approximately 60 nm thick. Figure 5.5 shows the IV characteristics of the InSe thin film.

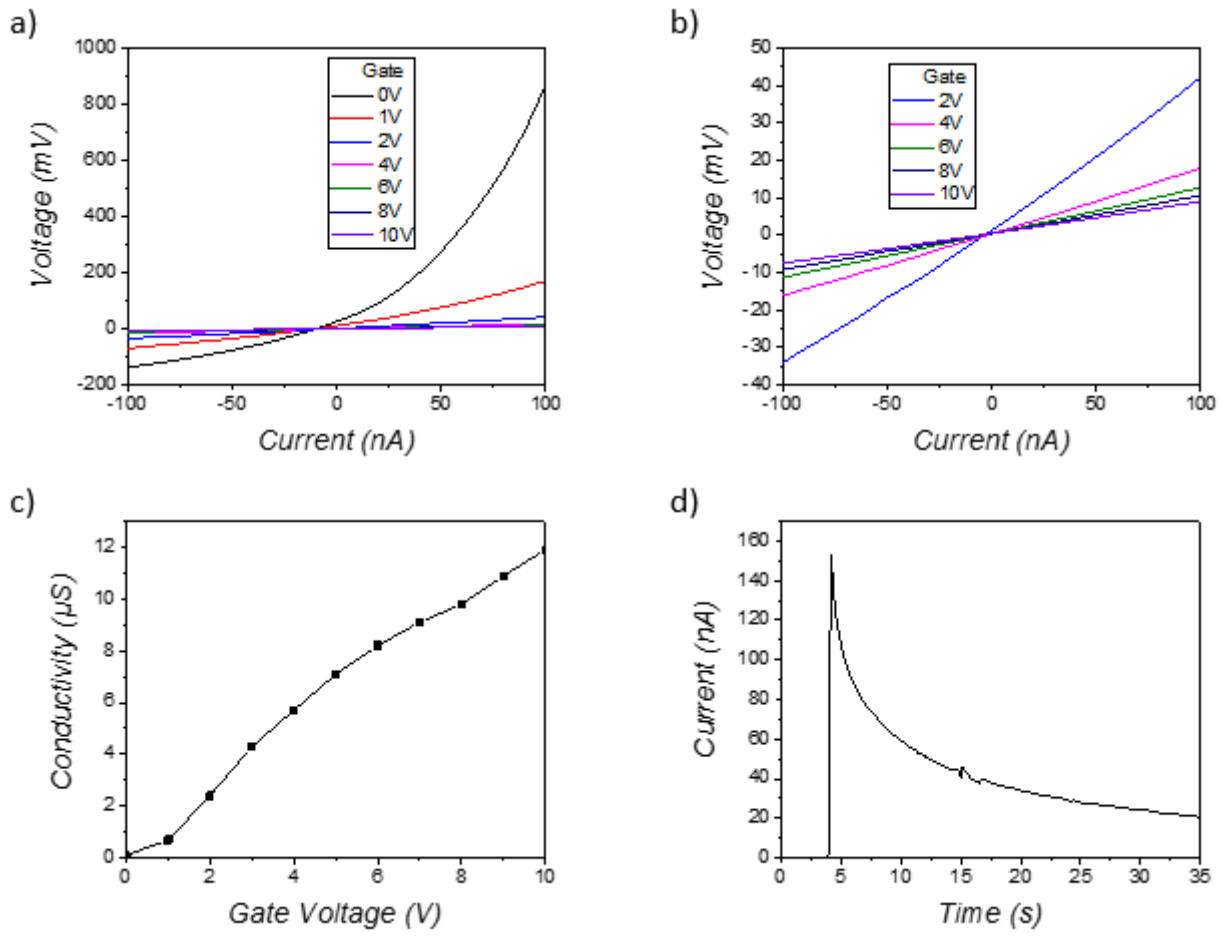

Figure 5.5: IV characteristics of InSe thin film a) IV curves with different gate voltages b) Plot a zoomed in with V_g = 0V and V_g = 1V suppressed c) Conductivity vs gate voltage d) Sustainability when V_g = 10V applied

Figure 5.5 c shows that the sample can be gated to increase the number of charge carriers. The conductivity is increase by a factor of 95 when a gate voltage of 10 V is applied. However, figure 5.5 d shows that the gate voltage effect is not sustainable in this sample, the gating effect decays over time. The initial conclusion is that there is bad contact between the InSe sample and PMMA substrate.

Despite the gate voltage effect not being sustainable, attempts were still made to induce and image a surface plasmon on the InSe sample. Figure 5.6 shows the attempt at inducing and imaging a surface plasmon while applying a gate bias of 10 V with incident light of 10.8 μm.

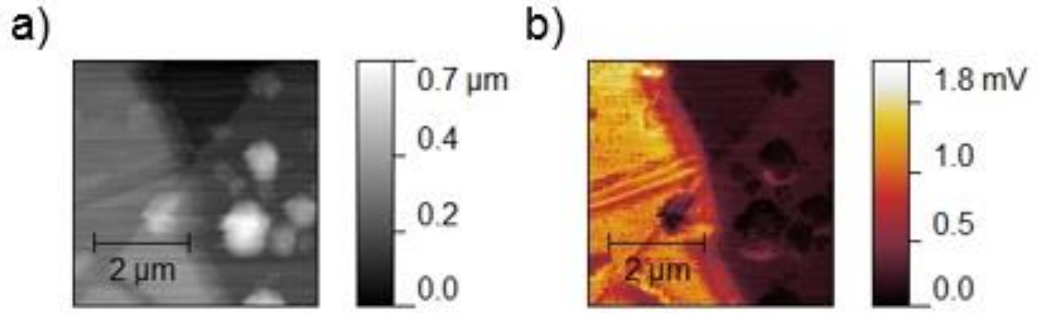

Figure 5.6: a) AFM topography of the InSe flake at electrode edge b) Near-field amplitude image of InSe flake at electrode edge while applying 10V gate bias

No surface plasmon was found in the near-field amplitude scan image. There is nothing indicating any fringe like patterns near any of the surface edges in the image. The decaying of the gate voltage effect would not sustain an increase of charge carriers in the InSe flake. These scans take approximately 1 hour to complete, and by the time the scan completed there is no gate effect taking place.

Attempts at inducing and imaging a surface plasmon on InSe thin film will continue. The next step is to obtain a sample that can sustain the gate voltage effect over long periods of time. This will allow for an increase in charge carriers throughout the InSe thin film that could assist in the generation of a surface plasmon. Au nanoparticles have been shown to enhance plasmonic effects [46]. They could be

incorporated onto the InSe flake once initial testing is complete to help induce a surface plasmon.

5.2. NbO_2

NbO_2 is an interesting material that undergoes an insulator to metal phase transition at 1080 K [47]. This high temperature phase transition gives application projections for NbO_2. Other materials exhibiting this phenomenon have the phase transition at or below room temperature making them not applicable for everyday technology [47].

It is known that NbO_2 has a structural change during this phase transition. In the low temperature insulating phase, it has a body centered, tetragonal, distorted rutile structure. Then at high temperatures it becomes metallic and has an undistorted rutile structure as shown in figure 5.7 [47].

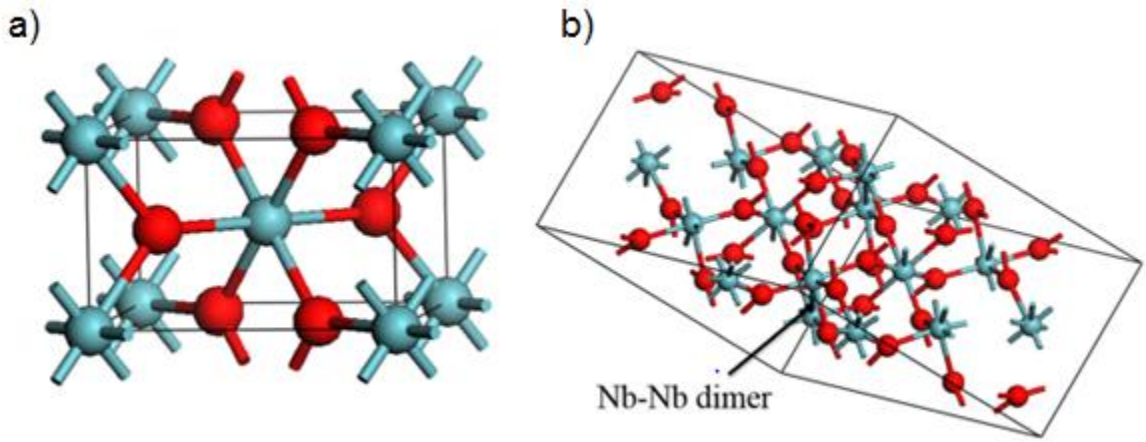

Figure 5.7: Crystal structure of NbO_2 in a) high temperature metallic phase b) low temperature insulating phase [47]

It is not well understood how this phase transition takes place. More in depth studies have been conducted on VO_2, a very similar compound to NbO_2. VO_2 has an insulator to metal phase transition at 340 K [48]. Metallic and insulating domains will have differences in their dielectric properties. It has been shown with VO_2 that s-SNOM images can be used to map out the domain structures of the two different phases [48]. S-SNOM images of VO_2 once heated above its transition temperature are shown in figure 5.8.

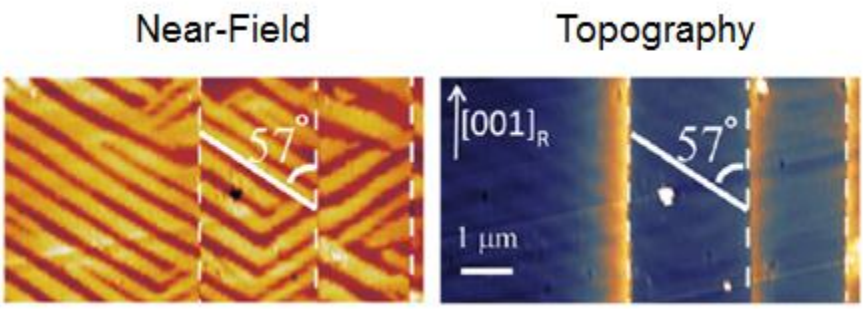

Figure 5.8: Near-field amplitude and topography scan images of VO_2 heated above the insulator to metal transition temperature [48]

It is evident in figure 5.8 that there are two different phases in the material. Also domains being formed clearly have orientation preference along a certain axis. The goal of this research is to gain insight on how the phase transition takes place in NbO_2. Near-field images will be taken on NbO_2 similar to figure 5.8. The idea is to compare domain structures in the near-field scans to the lattice structure, and also to determine how the phase transition initiates throughout the sample.

An NbO_2 sample grown on Al_2O_3 was supplied by graduate student, Toyanath Joshi at West Virginia University. The NbO_2 film is 20 nm thick [49]. The insulator to

metal transition is shown in figure 5.9 by a typical IV curve. A current is applied to heat the sample.

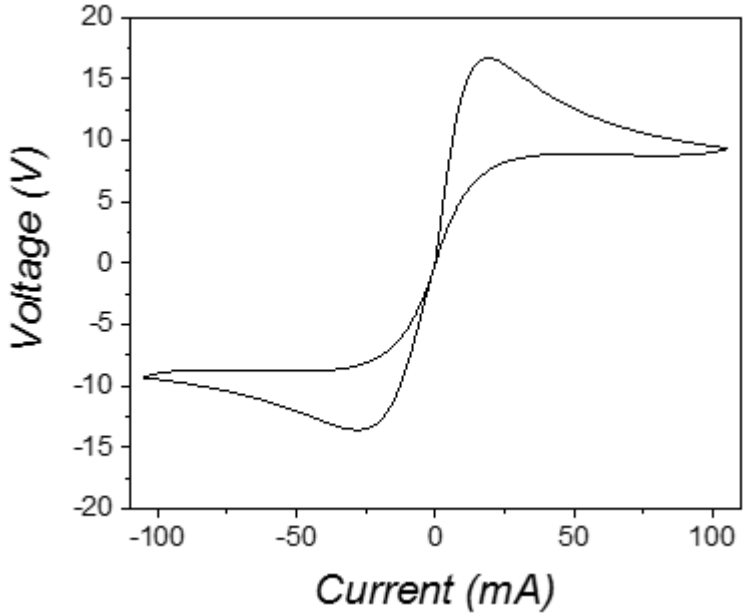

Figure 5.9: IV curve of NbO_2 on Al_2O_3 in air

It can be seen in figure 5.9 that there is a drastic change in resistance around 16.5 V showing the phase transition. The sequence of the IV curve shown is applying current in the sequence of 0 mA → 105 mA, 105 mA → -105 mA, and -105 mA → 0 mA. What is interesting about this plot is there is not enough voltage to heat the entire sample to 1080 K. The question arises, how does the phase transition initiate then? The idea in mind is that local heating of an area may form a small metallic area or conducting filament. Then this area would concentrate the heating, and this domain will spread. S-SNOM will be used to try and image the formation of any metallic structures in the NbO_2 film.

Kelvin probe force microscopy and magnetic force microscopy were run on this sample below and above the transition voltage. No conclusive indications of any domain structures were seen forming in the NbO_2. This research endeavor is still in the preliminary stages. The next step is to take s-SNOM images to look for the domain structures forming. S-SNOM images provide much higher spatial resolutions than the previously tested forms of microscopy. With these images a description of the insulator to metal phase transition could be developed.

6. TROUBLESHOOTING

There were many problems encountered when building this s-SNOM system. In this chapter, a few of the major issues that were encountered will be mentioned, and the solutions to these issues. Hopefully, these challenges can then be avoided for future groups building an s-SNOM system.

In the optical setup of this s-SNOM system, a large percentage of the initial light is lost at various places along the optical path. In the high vacuum chamber, when light is first focused by the lens, nearly half of light is blocked by the body of the AFM on the way to the elliptical mirror.

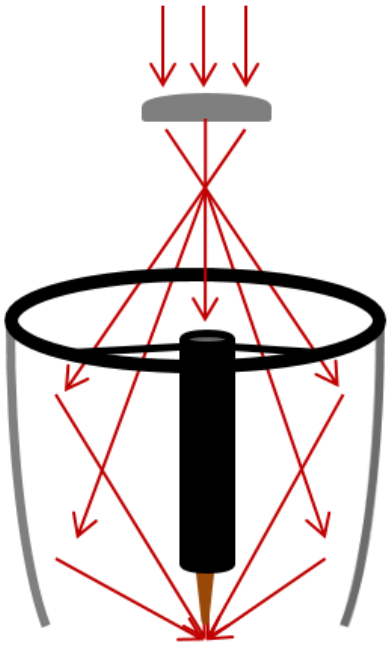

Figure 6.1: Light focused in high vacuum chamber being blocked by AFM

The initial plan was to use an axicon to avoid this loss of light. The idea was to create a ring of light before the high vacuum chamber. The center of the light is what is blocked by the AFM. By creating a ring, all the light could entirely be focused around the AFM. The idea of the axicon is depicted two dimensionally in figure 6.2.

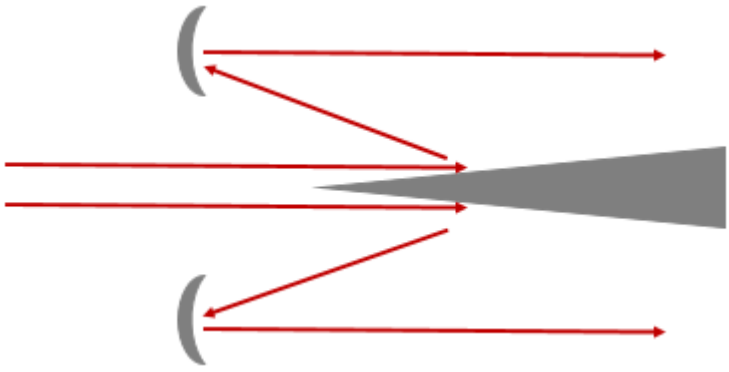

Figure 6.2: Axicon diverges the light and then collimates it again forming a ring of light

This seemed to be a great way to conserve more of the light through the optical path. The problem with this was on the return path of the light. Light naturally has a divergence no matter how well it is collimated. The divergence of the QCL was too great to allow the beam to pass back through the axicon unimpeded. The solution to this issue was to increase the beam diameter. The divergence of a beam increases with wavelength but is inversely proportional to the beam diameter, divergence α (λ / d) [37]. This is the purpose of the beam expander in the optical path. This helped the divergence issue, but now the beam is too large to pass through the axicon on the incident path. The increased beam diameter increases the amount of light that passes around the top of the AFM even without the axicon. This is the current state of the beam. A larger axicon could be employed to increase the overall amount of light reaching the near-field interaction point.

A second problem encountered was with the reference arm of the optics. It was stated in chapter 4 that there is a reference arm created at the beamsplitter for the pseudoheterodyne detection scheme. This reference arm is offset from the main arm and travels the same optical path to a planar mirror inside the high vacuum chamber. The initial intention was to just retroreflect the reference arm directly after the beamsplitter. This would be much easier to implement. However, retroreflecting after the beamsplitter always gave an interference signal between the two arms that was not stable. There would be phase shifting between the two arms. It was later concluded that this phase shifting was due to vibrations in the optics, specifically the mirror hanging inside the high vacuum chamber. The solution to this problem was to have the two arms

go through as identical of optical paths as possible. This did fix the instability of the interference.

A third problem was the control of the polarization of the light. Plasmons are polarization dependent so control has to be maintained. Initially hanging in the high vacuum chamber was an off axis parabolic mirror instead of the lens configuration that is there now. It was found that light going into the chamber polarized, was coming out not polarized as well. The polarization was not maintained, and the light that was polarized was rotated. Once investigated, it was realized that light being focused from an off axis parabolic mirror does have a small polarization rotation as shown in figure 6.3 [50].

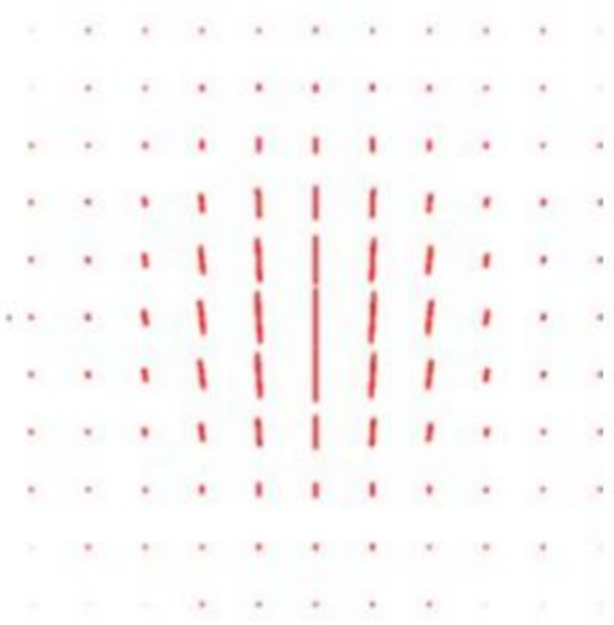

Figure 6.3: Profile of a focal point experiencing polarization rotation from an off axis parabolic mirror [50]

The rotation is very slight, but it increases away from the center of the beam. In this setup only the outer edges of the light are being used because the center is blocked by the AFM. Also, the light reflects off the off axis parabolic mirror twice which compounds the problem. The solution to this problem was changing the off axis parabolic mirror to a lens setup. A lens does not rotate the polarization of light.

One more issue that was encountered was the shorting of piezoelectric actuators. This happened several times and these actuators would need to be replaced. Once a voltage was applied to the actuator there could be leftover charge on them even after completion of its motion. If these actuators were disconnected from their ground, this left over charge can short the actuator. The solution to this was simple. If the actuator was going to be disconnected from its ground, first route any charge left on the actuator through a large resistor to dissipate the charge. Basically, just always discharge the actuators if they are going to be disconnected.

These are a few of the major issues that were encountered during the construction of this s-SNOM system. Future s-SNOM systems being designed and built should be cognizant of these problems that could arise and design accordingly.

7. CONCLUSION

This thesis has laid out the design and construction of a home built scattering type scanning near-field optical microscope. It contains a scanning optical microscope capable of recording far-field optical information. It focuses light onto a scanning sample surface and recollects the reflected light containing information using an interferometer setup. A second instrument within the setup is an atomic force microscope. The AFM is

used to measure forces between a scanning probe and the sample surface. The AFM records the topography of a sample surface simultaneously while running the s-SNOM system. These two instruments working in unison make up the s-SNOM system.

Light from the scanning optical microscope is focused to the same point that the AFM tip is taking measurements. The light is confined to the tip apex and creates an optical imaging device with spatial resolution below the diffraction limit of light. S-SNOM systems measure the interaction between the polarized tip and sample surface based on the dielectric properties of the sample. A change in the dielectric property within a scan image creates contrast between regions. This can be used for spectroscopy purposes looking for vibrational resonances within the material or for mapping out domain structures.

This s-SNOM system implements a pseudoheterodyne detection scheme to negate any unwanted background signal that could potentially cause artifacts within a scan image. It uses an elliptical mirror as the focusing objective drastically increasing the collection angle of light radiating from the tip compared to other s-SNOM systems. This unique s-SNOM system is variable temperature and high vacuum compatible. It also has the capability of applying electrical biases to the sample or tip.

Successful imaging of a surface plasmon at an Au and air interface has been demonstrated. This shows successful design and construction of this s-SNOM system. Research will continue to be carried out using this instrument. Attempts will be made to induce and image a surface plasmon on InSe thin films, and to image the phase transition taking place in NbO_2.

REFERENCES

[1] Ocelic, Nenad. *Quantitative Near-field Phonon-polariton Spectroscopy*. Thesis. 2007. N.p.: n.p., n.d.

[2] Pauling, L. 'Metal-Metal Bond Lengths In Complexes Of Transition Metals'. *Proceedings of the National Academy of Sciences* 73.12 (1976): 4290-4293.

[3] Greffet, Jean-Jacques, and Rémi Carminati. 'Image Formation In Near-Field Optics'. *Progress in Surface Science* 56.3 (1997): 133-237.

[4] Kwan, Alistair, John Dudley, and Eric Lantz. 'Who Really Discovered Snell's Law?'. *Physics World* 2002: 64. Web. 16 Sept. 2015.

[5] Bek, Alpan. 'APERTURELESS SNOM: A NEW TOOL FOR NANO-OPTICS'. M.Sc. Thesis. Bilkent University, 2004.

[6] Miles, Richard, Walter Lempert, and Joseph Forkey. 'Laser Rayleigh Scattering'. *Measurement Science and Technology* 12 (2001): 33-51.

[7] Hahn, David W. "Raman scattering theory." *Department of Mechanical and Aerospace Engineering, University of Florida* (2007).

[8] Turrell, George, and G. Corset. "The raman effect." *Raman Microscopy. Developments and Applications* (1996).

[9] "Raman Scattering." *Wikipedia*. Wikimedia Foundation, n.d. Web. 10 Oct. 2015. <https://en.wikipedia.org/wiki/Raman_scattering>.

[10] Gfroerer, Timothy H. "Photoluminescence in analysis of surfaces and interfaces." *Encyclopedia of Analytical Chemistry* (2000).

[11] "Properties of Piezo Actuators." *Piezo Technology*. N.p., n.d. Web.01 Oct. 2015. <http://www.piceramic.com/piezo-technology/properties-piezo-actuators.html>.

[12] Yeo, Woon Seung, and Jonathan Berger. *Raster Scanning: A New Approach to Image Sonification, Sound Visualization, Sound Analysis, and Synthesis*. Diss. Department of Music, Stanford University, 2008.

[13] Lauterbach, Marcel A. "Finding, defining and breaking the diffraction barrier in microscopy–a historical perspective." *Optical Nanoscopy* 1.1 (2012): 8.

[14] Mariani, Stefano, et al. "Investigating nanoparticle properties in plasmonic nanoarchitectures with DNA by surface plasmon resonance imaging." *Chemical Communications* 51.30 (2015): 6587-6590.

[15] Seddon, Angela B. "Mid-infrared (IR)–A hot topic: The potential for using mid-IR light for non-invasive early detection of skin cancer in vivo." *physica status solidi (b)* 250.5 (2013): 1020-1027.

[16] Brar, Victor W., et al. "Highly confined tunable mid-infrared plasmonics in graphene nanoresonators." *Nano letters* 13.6 (2013): 2541-2547.

[17] "Material Data." *Rocky Mountain Instruments*. N.p., n.d. Web. 03 June 2015. <http://rmico.com/support/tech-notes/material-data>.

[18] Liu, Jian, et al. "Focusing of an elliptical mirror based system with aberrations."*Journal of Optics* 15.10 (2013): 105709.

[19] Hutter, Jeffrey L., and John Bechhoefer. "Calibration of atomic-force microscope tips." *Review of Scientific Instruments* 64.7 (1993): 1868-1873.

[20] Hrouzek, Michal. "Atomic Force Microscopy, Modeling, Estimation and Control." Thesis. Universite Joseph Fourier-Grenoble, 2007.

[21] Meyer, E. R. N. S. T. "Atomic force microscopy." *Progress in surface science*41.1 (1992): 3-49.

[22] Garcia, Ricardo, and Alvaro San Paulo. "Attractive and repulsive tip-sample interaction regimes in tapping-mode atomic force microscopy." *Physical Review B* 60.7 (1999): 4961.

[23] Pruthi, Meenu, and Anurag Singh. "Analysis and study of Quality factor for simple fixed beam mems Resonator." *International Journal of Engineering Research and General Science* 2.4 (2014).

[24] Lübbe, Jannis, et al. "Achieving high effective Q-factors in ultra-high vacuum dynamic force microscopy." *Measurement Science and Technology* 21.12 (2010): 125501.

[25] Hillenbrand, R., B. Knoll, and F. Keilmann. "Pure optical contrast in scattering-type scanning near-field microscopy." *Journal of microscopy* 202.1 (2001): 77-83.

[26] Keilmann, Fritz, and Rainer Hillenbrand. "Near-field microscopy by elastic light scattering from a tip." *PHILOSOPHICAL TRANSACTIONS-ROYAL SOCIETY OF LONDON SERIES A MATHEMATICAL PHYSICAL AND ENGINEERING SCIENCES* (2004): 787-806.

[27] Chen, Weibin, and Qiwen Zhan. "Numerical study of an apertureless near field scanning optical microscope probe under radial polarization illumination."*Optics express* 15.7 (2007): 4106-4111.

[28] Cvitkovic, A., N. Ocelic, and R. Hillenbrand. "Analytical model for quantitative prediction of material contrasts in scattering-type near-field optical microscopy." *Optics express* 15.14 (2007): 8550-8565.

[29] Redzic, Dragan V. "An Electrostatic Problem: A Point Charge outside a Prolate Dielectric Spheroid." *Am. J. Phys. American Journal of Physics* 62.12 (1994):1118.

[30] Lindell, I. V., G. Dassios, and K. I. Nikoskinen. "Electrostatic image theory for the conducting prolate spheroid." *Journal of Physics D: Applied Physics* 34.15 (2001): 2302.

[31] Huber, A., et al. "Nanoscale resolved infrared probing of crystal structure and of plasmon-phonon coupling." *Nano letters* 6.4 (2006): 774-778.

[32] Ocelic, Nenad, Andreas Huber, and Rainer Hillenbrand. "Pseudoheterodyne detection for background-free near-field spectroscopy." *Applied Physics Letters*89.10 (2006): 101124.

[33] Stiegler, Johannes M. "Infrared Spectroscopic Near-field Microscopy of Nanoparticles and Semiconductor Nanowires." Thesis. Euskal Herriko Unibersitea – Universidad Del Pais Vasco, 2012.

[34] Enoch, Stefan, and Nicolas Bonod, eds. *Plasmonics: from basics to advanced topics*. Vol. 167. Springer, 2012.

[35] Zhang, Junxi, Lide Zhang, and Wei Xu. "Surface plasmon polaritons: physics and applications." *Journal of Physics D: Applied Physics* 45.11 (2012): 113001.

[36] Pitarke, J. M., et al. "Theory of surface plasmons and surface-plasmon polaritons." *Reports on progress in physics* 70.1 (2007): 1.

[37] Zangwill, Andrew. *Modern electrodynamics*. Cambridge University Press, 2013.

[38] Johnson, Peter B., and R-W_ Christy. "Optical constants of the noble metals."*Physical Review B* 6.12 (1972): 4370.

[39] Bastian, S. "Notes on electromagnetic waves in a plasma." *National Radio Astronomy Obsevatory, Charlottesville, VA* (2005).

[40] Li, Hongjian, et al. "Tunable plasmon resonance wavelength of the periodic gold film with converging and diverging shaped slits and grooves." *Solid State Communications* 151.2 (2011): 159-163.

[41] Fei, Zhe, et al. "Gate-tuning of graphene plasmons revealed by infrared nano-imaging." *Nature* 487.7405 (2012): 82-85.

[42] Marshall, Joseph M., and Doriana Dimova-Malinovska, eds. *Photovoltaic and Photoactive Materials: Properties, Technology and Applications*. Vol. 80. Springer Science & Business Media, 2012.

[43] Yao, Wenjie, et al. "Efficient Directional Excitation of Surface Plasmons by a Single-Element Nanoantenna." *Nano letters* 15.5 (2015): 3115-3121.

[44] Lei, Sidong, et al. "Evolution of the electronic band structure and efficient photo-detection in atomic layers of InSe." *ACS nano* 8.2 (2014): 1263-1272.

[45] Benramdane, N., et al. "Optical constants of InSe and In 4 Se 3 thin films in the far infrared region." *Microelectronic Engineering* 51 (2000): 645-657.

[46] Atwater, Harry A., and Albert Polman. "Plasmonics for improved photovoltaic devices." *Nature materials* 9.3 (2010): 205-213.

[47] O'Hara, Andrew, et al. "Electronic and optical properties of NbO2." *Journal of Applied Physics* 116.21 (2014): 213705.

[48] Liu, Mengkun, et al. "Symmetry breaking and geometric confinement in VO2: Results from a three-dimensional infrared nano-imaging." *Applied Physics Letters* 104.12 (2014): 121905.

[49] Joshi, Toyanath, et al. "Preparation, characterization, and electrical properties of epitaxial NbO2 thin film lateral devices." *Journal of Physics D: Applied Physics* 48.33 (2015): 335308.

[50] Sung, Shijun, et al. "THz optical design considerations and optimization for medical imaging applications." *SPIE Optical Engineering+ Applications*. International Society for Optics and Photonics, 2014.